Strain and Defect-Tailored Magnetotransport in $NiCo_2O_4$ Thin Films and Freestanding Membranes

Qiuchen Wu,[1] Yuanyuan Zhang,[1] Tianlin Li,[1] Myung-Geun Han,[2] Soo-Yoon Hwang,[2,3] Yeon-Seo Nam,[2,3] Si-Young Choi,[3] Yimei Zhu,[2] and Xia Hong[1,*]

[1] Department of Physics and Astronomy & Nebraska Center for Materials and Nanoscience, University of Nebraska–Lincoln, Lincoln, NE 68588-0299, USA

[2] Condensed Matter Physics and Materials Science Department, Brookhaven National Laboratory, Upton, NY 11973-5000, USA

[3] Department of Materials Science and Engineering, Pohang University of Science and Technology (POSTECH), Pohang 37673, Republic of Korea

[*] Author to whom correspondence should be addressed: xia.hong@unl.edu

ABSTRACT:

Magnetic spinel oxides are high-performance spintronic materials due to their high Curie temperature, high spin polarization, fast spin dynamics, and strain tunable magnetic anisotropy. Epitaxial strain and disorder can significantly modify the electronic and magnetic energy landscape, while their interplay remains elusive. Here we use epitaxial $NiCo_2O_4$ thin films and freestanding $NiCo_2O_4$ membranes as model systems to reveal the complex roles of strain and defects in determining the metallicity and magnetotransport properties of the ferrimagnetic spinel. Unlike the perpendicular magnetic anisotropy and two-fold sinusoidal anisotropic magnetoresistance (AMR) observed in metallic $NiCo_2O_4$ films on spinel substrates, $NiCo_2O_4$ on perovskite substrates and $NiCo_2O_4$ membranes exhibit insulating behaviors and spin canting, with an additional four-fold AMR component emerging due to disorder-induced spin scattering and strain-induced tetragonal magnetocrystalline anisotropy. The amplitude ratio between the four-fold and two-fold AMR components provides critical information of the disorder types that contribute to the AMR. Electron microscopy studies reveal structural and chemical phase separation in the membranes similar to those in disordered films, which explains the highly consistent magnetotransport properties for $NiCo_2O_4/Sr_3Al_2O_6$ films and $NiCo_2O_4$ membranes. Our study provides effective material strategies for engineering spin transport and magnetic anisotropy in $NiCo_2O_4$ and presents a promising venue for designing flexible magnetic memory, sensor, and spintronic applications.

KEYWORDS: *freestanding spinel membranes, anisotropic magnetoresistance, magnetocrystalline anisotropy, anomalous Hall effect, phase separation*

Magnetic spinel oxides are promising spintronic materials due to their high Curie temperature (T_C), high spin polarization, and large magnetoelastic effects.[1-3] Among them, the ferrimagnetic $NiCo_2O_4$ (NCO) exhibits above room temperature T_C,[4-6] potential half metallicity,[7] fast spin dynamics,[8] and strain tunable magnetic anisotropy.[9] It has been shown that epitaxial $NiCo_2O_4$ films possess superior conductivity and sustain magnetic order down to sub-two-unit-cell thickness.[6, 10] The strong perpendicular magnetic anisotropy (PMA)[3] and various magnetotransport anomalies[5, 11] observed in $NiCo_2O_4$ on spinel $MgAl_2O_4$ (MAO) substrates make it appealing for developing novel magnetic devices, such as linear magnetoresistance (MR)-based magnetic sensors and anomalous Hall effect (AHE)-based nonvolatile memories.[3] Due to the complex crystal structure and the multi-cation, mixed-valence nature, spinel oxides are prone to formation of various structural and chemical disorders.[12] These properties are advantageous for energy storage and catalysis applications,[2, 13] and polymorphous spinel nanostructures have been extensively investigated to enhance the ratio between defective surface and sample volume.[14-17] For epitaxial thin films of $NiCo_2O_4$, on the other hand, these disorders can compromise the magnetic order,[6, 10] modify the magnetic energy landscape,[12] and induce unconventional transport responses such as phase-separation induced magnetoresistance,[18] quadruple anomalous Hall effect,[11] and potential altermagnetism.[19] The strain and disorder effects are closely intertwined in determining the electronic and magnetic properties of $NiCo_2O_4$ thin films. The ability to tailor their individual contributions is critical for understanding the emergent spin phenomena and designing $NiCo_2O_4$-based magnetic applications, while their interplay remains elusive.

Recent advancements in the synthesis of freestanding oxide membranes present a unique venue to separate the effects of epitaxial strain and disorder.[20] Previous studies of complex oxide membranes have focused on perovskite oxides,[21-22] which lead to the observation of flexoelectric effect[23] and interface tunable coercivity and domain wall roughness in $Pb(Zr,Ti)O_3$,[24] emergent polar states in $SrTiO_3$ (STO)[25] and $SrRuO_3$,[26] and stacking induced oxide moiré structures,[27-28] as well as enabling various flexible device applications, such as ferroelectric-gated 2D transistors,[24, 29] optoelectronics,[30] and ferroelectric tunnel junctions.[31-32] The membrane forms of spinel oxides,

despite the strong fundamental interests and high technological potential, have been rarely explored.[33-34]

In this work, we report the realization of spinel oxide membranes, using epitaxial $NiCo_2O_4$ films and $NiCo_2O_4$ membranes as model systems to assess the strain and defect effects on the magnetotransport properties. We synthesize 30 nm (001) $NiCo_2O_4$ thin films on various substrates, including spinel $MgAl_2O_4$, perovskite $SrTiO_3$ and $LaAlO_3$ (LAO), and $Sr_3Al_2O_6$ (SAO) buffered $LaAlO_3$, and fabricate freestanding $NiCo_2O_4$ membranes via water etching of the $Sr_3Al_2O_6$ buffer layer. $NiCo_2O_4$ films on lattice compatible $MgAl_2O_4$ substrates exhibit metallic behavior, strong PMA, and two-fold sinusoidal in-plane anisotropic magnetoresistance (AMR). In contrast, $NiCo_2O_4$ prepared on perovskite substrates show insulating behavior and canted spin, with an additional four-fold AMR component emerging at low temperatures, which can be attributed to disorder-induced spin scattering and strain-induced tetragonal magnetocrystalline anisotropy (MCA). The amplitude ratio between the four-fold and two-fold AMR components provides critical information of the disorder types that contribute to the AMR. The $NiCo_2O_4$ membrane exhibits highly consistent transport behaviors with those of the unsuspended $NiCo_2O_4/Sr_3Al_2O_6$ film, indicating that the strain and disorder levels are mostly preserved after suspension. The transport results have been corroborated with comprehensive transmission electron microscopy (TEM) studies of $NiCo_2O_4$ membranes, which reveal structural and chemical phase separation similar to those reported in highly disordered $NiCo_2O_4$ films. Our study presents a promising venue to achieve functional design of crystalline $NiCo_2O_4$ at the nanoscale, paving the path for their implementation in flexible electronic, magnetic, and spintronic applications.

RESULTS

Sample Preparation and Characterization

We deposit 30 nm epitaxial (001) $NiCo_2O_4$ thin films on $MgAl_2O_4$, $SrTiO_3$, and $LaAlO_3$ substrates, where $NiCo_2O_4$ is subjected to 0.38%, 3.7%, and 6.6% compressive strain, respectively. The sample thickness is chosen to optimize the signal-to-noise ratio for magnetotransport studies. The details of sample preparation and characterization can be found in the Methods and Supporting Information (SI). X-ray diffraction (XRD) θ-2θ scans indicate epitaxial (001) growth of all films with no apparent impurity peaks (Figure 1a and SI Figure S1). The *c*-axis lattice constants of $NiCo_2O_4$ are 8.196 Å on $MgAl_2O_4$, 8.207 Å on $SrTiO_3$, and 8.165 Å on $LaAlO_3$, higher than the

bulk value (8.114 Å), which is consistent with the compressive strain. Atomic force microscopy (AFM) measurements reveal smooth surface morphology of the $NiCo_2O_4$ films with root-mean-squared (RMS) roughness of 2-6 Å (Figure 1a and SI Figure S1). To fabricate $NiCo_2O_4$ membranes, we deposit 30 nm $NiCo_2O_4$ on 10 nm $Sr_3Al_2O_6$ buffered $LaAlO_3$ substrates (Figure 1b) followed by water etching. XRD θ-2θ scans show epitaxial (001) growth of NCO/SAO (Figure 1a) with *c*-axis lattice constant of 8.187 Å for $NiCo_2O_4$. After water etching, the suspended $NiCo_2O_4$ layer is laid on $LaAlO_3$ substrate and dried. XRD characterizations confirm that the peaks for the $Sr_3Al_2O_6$ buffer layer have disappeared, while the suspended $NiCo_2O_4$ membrane retains the crystallinity (Figure 1a and SI Figure S2). The *c*-axis lattice constant of $NiCo_2O_4$ membrane is 8.170 Å, which is comparable with that of NCO/LAO. The strain states of the samples are further analyzed via reciprocal space mapping (RSM). As shown in SI Figure S3, the $NiCo_2O_4$ film on $MgAl_2O_4$ remains fully strained, while $NiCo_2O_4$ on the perovskite substrates and the $NiCo_2O_4$ membrane are partially relaxed. The deduced lattice constants are given in SI Table S1. AFM measurements show that the surface roughness of NCO/SAO is about 2 Å, which increases to about 6 Å in the membrane. The suspended membrane sample is smooth over large scales with few cracks (SI Figure S4), and the increased surface roughness has been widely observed in oxide membranes, which might be due to the surface rippling effect and/or inhomogeneous strain distribution.[23-24, 35]

Selected $NiCo_2O_4$ membrane areas are picked up by Gel-Film and transferred onto a TEM grid (SI Figure S5). Figure 1c-h shows the high-angle annular dark-field scanning TEM (HAADF-STEM) images and electron energy loss spectroscopy (EELS) element maps taken on a membrane sample, which reveal two types of structural phases and small patches of bright regions (Figure 1c). The red boxed region in Figure 1d possesses an ideal inverse spinel structure of $NiCo_2O_4$. Fast Fourier transform (FFT) analysis shows all the (040), (400), and (220) reflections (Figure 1e). EELS element mapping shows that the Ni ions occupy the B-sites and the Co ions are distributed in both A-sites and B-sites (Figure 1f), as expected for the inverse spinel structure $[Co_A(Ni,Co)_BO_4]$. In contrast, the blue boxed region in Figure 1d hosts an imperfect unit cell with A-site cation missing, as revealed by the HAADF-STEM image (Figure 1g) and EELS maps (Figure 1h). The corresponding FFT shows the (220) reflections patterns are missing. The EELS maps further confirm the absence of A-site Co ions (Figure 1h and SI Figure S6). Similar structural phase separation has been reported in films on rock-salt substrates[18] or subjected to spinodal decomposition.[36] The phase separation can be attributed to the distinct crystal structure (space

group $Fd\bar{3}m$ for $NiCo_2O_4$ and $Pa\bar{3}$ for $Sr_3Al_2O_6$) and strain relaxation. In contrast, (001) $NiCo_2O_4$ films deposited on $MgAl_2O_4$ substrates are structurally homogeneous without defect phases[5-6] due to the compatible crystal structure and coherent strain level (SI Figure S3). In addition, EELS mapping of the bright patch region reveals the absence of Co, which is attributed to the formation of NiO (Figure S7). As NiO has much larger accumulated Z-contrast per column compared with that of either A-site or B-site columns in $NiCo_2O_4$, it yields a brighter HAADF-STEM signal (SI Section 3). This chemical phase segregation has been widely observed in $NiCo_2O_4$ thin films[37] and nanostructures[38] as NiO is thermodynamically more stable.[3]

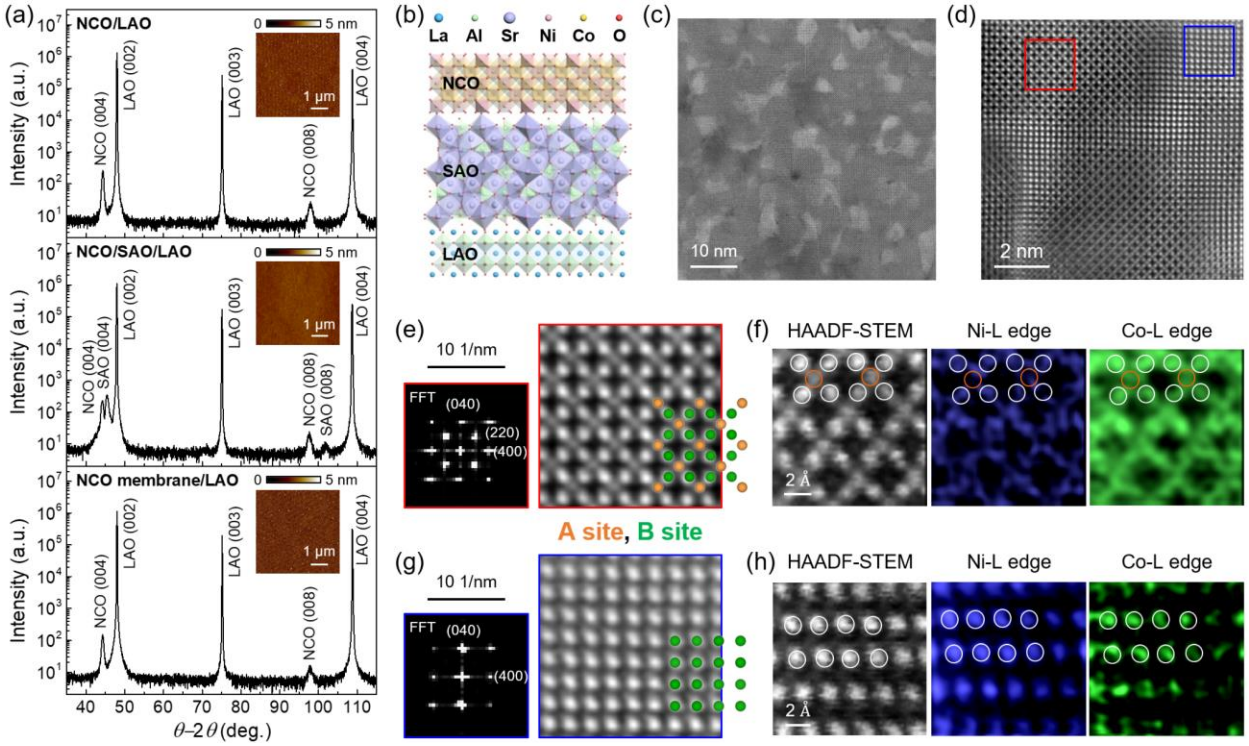

Figure 1. Characterizations of 30 nm $NiCo_2O_4$ thin films and membranes. (a) XRD θ–2θ scans of NCO film on LAO substrate (top), NCO film on 10 nm SAO buffered LAO substrate (middle), and suspended NCO membrane on LAO substrate after water etching of SAO buffer layer (bottom). Insets: AFM topography images. (b) Schematic of NCO/SAO/LAO. (c, d) HAADF-STEM images of NCO membrane along (001) direction with (c) low and (d) high magnification. (e) Enlarged image of the red boxed region in (d) and the corresponding FFT (left inset). (f) HAADF-STEM image and EELS maps for Ni-L and Co-L edges taken on the inverse spinel region. (g) Enlarged image of the blue boxed region in (d) and the corresponding FFT (left inset). (h) HAADF-STEM image and EELS maps for Ni-

L and Co-L edges taken on the A-site missing region. The A sites are labeled as orange dots/circles, and the B sites are labled as green dots/white circles in (e)-(h).

Transport and Magnetotransport Properties

The strain state and substrate crystal structure have profound effects on the transport properties of $NiCo_2O_4$. Figure 2a shows the temperature dependence of resistivity $\rho(T)$ for the $NiCo_2O_4$ films and membrane. For $NiCo_2O_4$ on $MgAl_2O_4$, ρ exhibits weak temperature dependence with metallic behavior ($d\rho/dT > 0$) above 35 K followed by a slight resistivity upturn below 35 K, consistent with previous reports.[5-6] The minimum resistivity value of $\rho_{\min}(35\ \mathrm{K}) = 0.61\ \mathrm{m\Omega\ cm}$ is among the best results reported for epitaxial $NiCo_2O_4$ films.[4-6, 10, 37, 39-40] In contrast, $NiCo_2O_4$ films on $SrTiO_3$, $LaAlO_3$, and $Sr_3Al_2O_6$ buffered $LaAlO_3$ are significantly more resistive and exhibit insulating behavior ($d\rho/dT < 0$) over the entire temperature range. Due to the larger compressive strain and the distinct crystal structures between $NiCo_2O_4$ and the perovskite substrates, these samples are strain relaxed and can host high density defects such as structural/chemical phase separation[18] and antiphase boundaries.[3] It is interesting to note that the $NiCo_2O_4$ membrane shows almost identical $\rho(T)$ as that of the $NiCo_2O_4$ film on $Sr_3Al_2O_6$ buffered $LaAlO_3$. This confirms that water etching does not introduce additional defects and the membrane sustains most of the strain level, corroborating the XRD results (Figure 1a and SI Figure S2-3). The temperature dependence of conductivity for the insulting samples can be well described by considering the contributions from thermal activation, nearest-neighbor hopping (NNH), and three-dimensional (3D) variable range hopping (VRH) (Figure 2b and SI Figure S8):

$$\sigma(T) = \sigma_0 \exp\left(-\frac{E_A}{k_B T}\right) + \frac{c_{NN}}{T}\exp\left(-\frac{T_{NN}}{T}\right) + \sigma_{VR} exp\left[-\left(\frac{T_{VR}}{T}\right)^{\frac{1}{4}}\right]. \quad (1)$$

Here σ_0, c_{NN}, and σ_{VR} are fitting parameters, E_A is the thermal activation energy, and T_{NN} and T_{VR} are the characteristic temperatures for nearest-neighbor hopping and variable range hopping, respectively. The two hopping models have previously been used to explain the insulating behavior of micron-sized $NiCo_2O_4$ nanoplates[41] and $NiCo_2O_4$ thin films grown on Al_2O_3 substrates.[37] The fitting parameters are summarized in SI Table S2. As shown in Figure 2b inset, the conduction is dominated by nearest-neighbor hopping at high temperatures and 3D variable range hopping at low temperatures, while thermally activated conduction only becomes important in the intermediate temperature range. Overall, the samples show relatively small variation in E_A (4.3-

8.6 meV) and T_{NN} (500-715 K). Despite the similar strain level, the NCO/SAO film and $NiCo_2O_4$ membrane show more than two orders of magnitude higher T_{VR} (> 200 K) than that of NCO/LAO (1.8 K), which corresponds to three-to-four orders of magnitude higher density of defect states at the Fermi level $N(E_F)$ and substantially smaller localization length (SI Section 4). This result suggests that the crystal structure of the interfacial $Sr_3Al_2O_6$ layer plays a dominant role in determining the localized transport behavior. For comparison, ultrathin $NiCo_2O_4$ film on $MgAl_2O_4$ also exhibits an insulating state due to the finite size effect, while $\sigma(T)$ of a 1.2 nm $NiCo_2O_4$ (1.5 unit cell) can be fully accounted for by nearest-neighbor hopping and thermal activation, with a larger E_A of 30 meV and a lower T_{NN} of 135 K. The distinct thermal activation energies point to the different origins for the insulating behaviors in thick $NiCo_2O_4$ on perovskite substrates and ultrathin $NiCo_2O_4$ on $MgAl_2O_4$. The former can be attributed to phonon assisted de-trapping of charged mobile defects,[42] while the latter suggests the emergence of a correlation gap due to quantum confinement.[43]

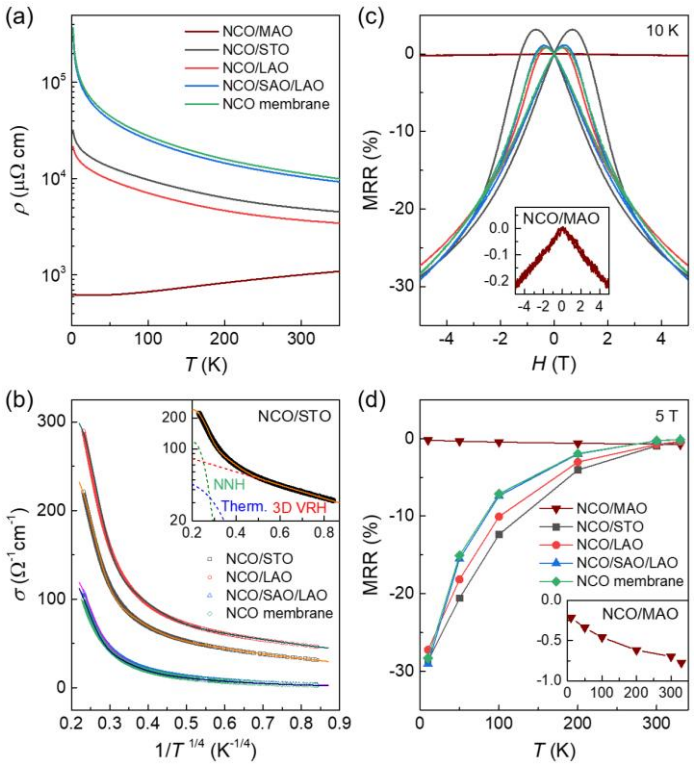

Figure 2. Temperature-dependence of transport properties of $NiCo_2O_4$ films and membrane. (a) $\rho(T)$. (b) $\sigma(T)$ of NCO/STO, NCO/LAO, NCO/SAO/LAO, and NCO membrane (open symbols) with fits (solid lines). Inset: Overall fit to the data for NCO/STO (solid line) with individual contributions of NNH, thermal activation, and 3D VRH (dashed lines). (c) MRR vs H at 10 K. Inset: Expanded view of

MRR(H) for NCO/MAO. (d) MRR vs T at 5 T. Inset: Expanded view of MRR(T) for NCO/MAO. All data have the same color coding.

Next, we compare the magnetotransport properties of the metallic and disordered $NiCo_2O_4$ samples. Figure 2c shows the magnetoresistance ratio, defined as $\text{MRR} = [\rho(H) - \rho(0)]/\rho(0)$, as a function of out-of-plane magnetic field H at 10 K. The metallic $NiCo_2O_4$ film on $MgAl_2O_4$ shows a negative MR with linear field dependence, which reaches about -0.2% at 5 T (Figure 2c inset). The linear MR remains small over the entire temperature range with its magnitude decreasing with decreasing temperature (Figure 2d), which is the signature behavior of band-intrinsic Berry phase dominated effect,[44] attesting to the high sample quality with low defect density.[5] For $NiCo_2O_4$ samples exhibiting insulating behavior, MRR(H) shows a wide butterfly-shape hysteresis, which signals canted magnetization rotating to out-of-plane direction in low magnetic fields. This is in sharp contrast to $NiCo_2O_4$ on $MgAl_2O_4$, where the strong PMA leads to abrupt resistance switching upon magnetization reversal.[5] The MRR magnitude is significantly higher and increases with decreasing temperature, reaching 30% at 5 T and 10 K. Previous studies have suggested the large MRR can be attributed to the presence of disorder such as structural phase separation[18] or antiphase boundaries.[37, 45]

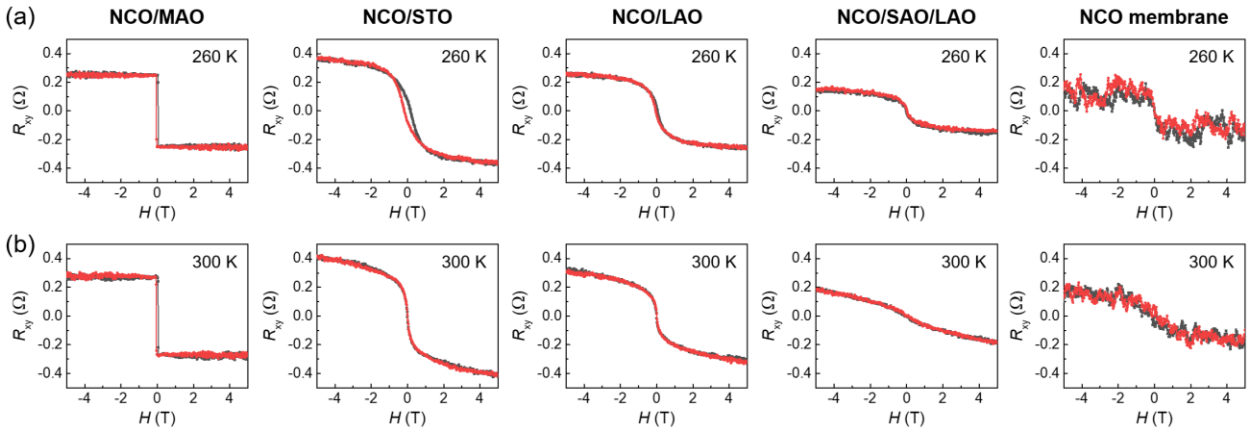

Figure 3. AHE of $NiCo_2O_4$ thin films and membrane in upsweep (black) and downsweep (red) magnetic fields. (a) R_{xy} vs H at 260 K. (b) R_{xy} vs H at 300 K.

Figure 3 shows the Hall resistance R_{xy} vs H taken on the samples. All samples exhibit the nonlinear, anomalous Hall component at 300 K, revealing above room temperature magnetic T_C. The AHE for $NiCo_2O_4$ on $MgAl_2O_4$ shows square-shape hysteresis due to the strong PMA (SI

Figure S9).[3, 5-6] All other samples exhibit slanted AHE hysteresis corresponding to canted spin orientation with a finite in-plane magnetization. Previous studies have shown that anti-site Ni^{3+} disorder can lead to canted magnetic moments on the A-site.[46] The shape of MR is also consistent with spin rotation in a perpendicular magnetic field (Figure 2c).[5] For NCO/SAO/LAO and $NiCo_2O_4$ membrane, the AHE resistance at 300 K is substantially suppressed compared with that at 260 K, suggesting T_C of these two samples is close to room temperature. The AHE hysteresis is consistent with the magnetization data taken at the same temperatures (SI Figure S10). Furthermore, at 100 K, the magnetization of $NiCo_2O_4$ on $MgAl_2O_4$ reaches the fully saturated value of 2 μ_B/formula unit,[5] while the insulating $NiCo_2O_4$ samples show significantly smaller magnetization at high fields (5 T), consistent with the fact that antiphase boundaries make it difficult to saturate the magnetization.[47]

In-plane Anisotropic Magnetoresistance

The distinct field dependences of MR and AHE in different samples show that the change of disorder landscape modifies the magnetic anisotropy in $NiCo_2O_4$, which can be assessed by the anisotropic magnetoresistance.[48] In magnetic conductors, the AMR effect is manifested as a sinusoidal oscillation of longitudinal resistance depending on the angle φ between the magnetization (M) and current (I) directions due to spin-orbit interaction (Figure 4a inset). Figure 4a and SI Figure S11a show the in-plane AMR resistivity ρ_{AMR} vs θ at 5 T for $NiCo_2O_4$ on $MgAl_2O_4$, with θ the angle between the in-plane magnetic field (H) and I ([100]-axis). At high fields, magnetization follows the field direction, so that $\theta \approx \varphi$. For all temperatures, the sample exhibits a two-fold sinusoidal behavior $\rho_{AMR} = \Delta\rho_{ARM}\cos[2(\theta + 90°)]$ (Figure 4b inset and 4c). The amplitude of AMR resistivity $\Delta\rho_{ARM}$ decreases monotonically with increasing temperature (Figure 4b), which is consistent with the temperature dependence of the magnetization in $NiCo_2O_4$ on $MgAl_2O_4$.[5] Figure 4d and Figure S11b show ρ_{AMR} vs θ at 10 K, where the two-fold sinusoidal behavior is sustained down to 0.25 T (Figure 4e inset and 4f). $\Delta\rho_{AMR}$ increases with increasing magnetic field and saturates at 3 T (Figure 4e). Due to the strong PMA for $NiCo_2O_4$ films on $MgAl_2O_4$,[5-6, 9] the in-plane magnetization is solely induced by the in-plane magnetic field and follows coherent rotation. The saturation field of $\Delta\rho_{AMR}$ also agrees well with what is required to fully rotate the magnetization to the in-plane orientation.[3]

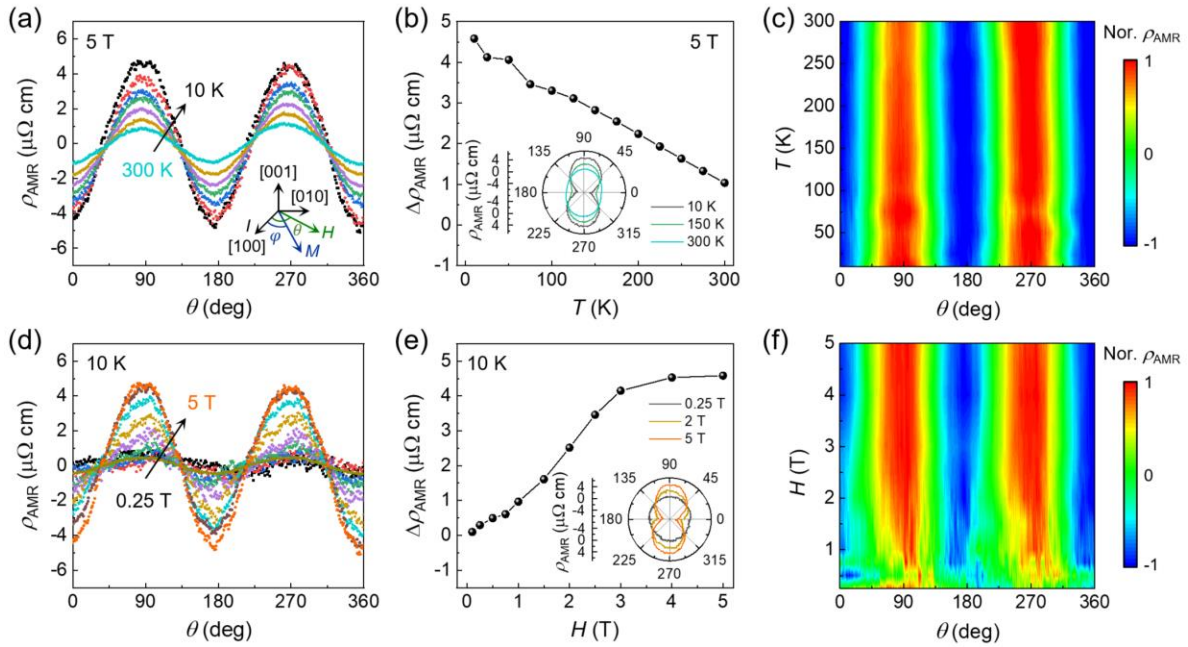

Figure 4. In-plane AMR of $NiCo_2O_4$ on $MgAl_2O_4$. (a) ρ_{AMR} vs θ at 5 T and various temperatures (300 K, 250 K, 200 K, 150 K, 100 K, 50 K, and 10 K). Inset: Schematic measurement setup. (b) $\Delta\rho_{AMR}$ vs T at 5 T. Inset: polar plots of ρ_{AMR} at 10, 150, and 300 K (c) Contour plot of normalized ρ_{AMR} vs θ and T at 5 T. (d) ρ_{AMR} vs θ at 10 K and various magnetic fields (0.25 T, 0.5 T, 0.75 T, 1 T, 1.5 T, 2 T, 2.5 T, 3 T, 4 T, and 5 T). (e) $\Delta\rho_{AMR}$ vs H at 10 K. Inset: polar plots of ρ_{AMR} at 0.25, 2, and 5 T. (f) Contour plot of normalized ρ_{AMR} vs θ and H at 10 K.

In contrast to the strong PMA in NCO/MAO, other $NiCo_2O_4$ samples possess canted magnetization with finite in-plane component (Figure 3 and SI Figure S10). The modified MCA leads to distinct symmetry in the in-plane AMR. For $NiCo_2O_4$ on $SrTiO_3$ at 300 K and 5 T, ρ_{AMR} still exhibits two-fold sinusoidal θ-dependence peaking at $\theta = 90°$ and 270° (SI Figure S12), which becomes distorted at 250 K (Figure 5a). At 200 K, additional peaks appear at $\theta = 0°$ and 180°, suggesting the emergence of a four-fold sinusoidal component. The angular dependence of ρ_{AMR} for all temperatures can be well described by:

$$\rho_{AMR}(\theta) = C_1 \cos(\theta + \theta_1) + C_2 \cos[2(\theta + \theta_2)] + C_4 \cos[4(\theta + \theta_4)] \quad (2)$$

where C_1, C_2, and C_4 are the one-fold, two-fold, and four-fold AMR coefficients, respectively. The four-fold component increases with decreasing temperature and becomes comparable with the two-fold component at 10 K (SI Figure S12). It has been theoretically predicted using a phenomenological model that the four-fold component arises from the high-rank resistivity tensor

of tetragonal MCA.[49-50] Another possible scenario for the four-fold symmetric AMR is related to the spin-dependent scattering near the anti-phase boundaries.[51-52]

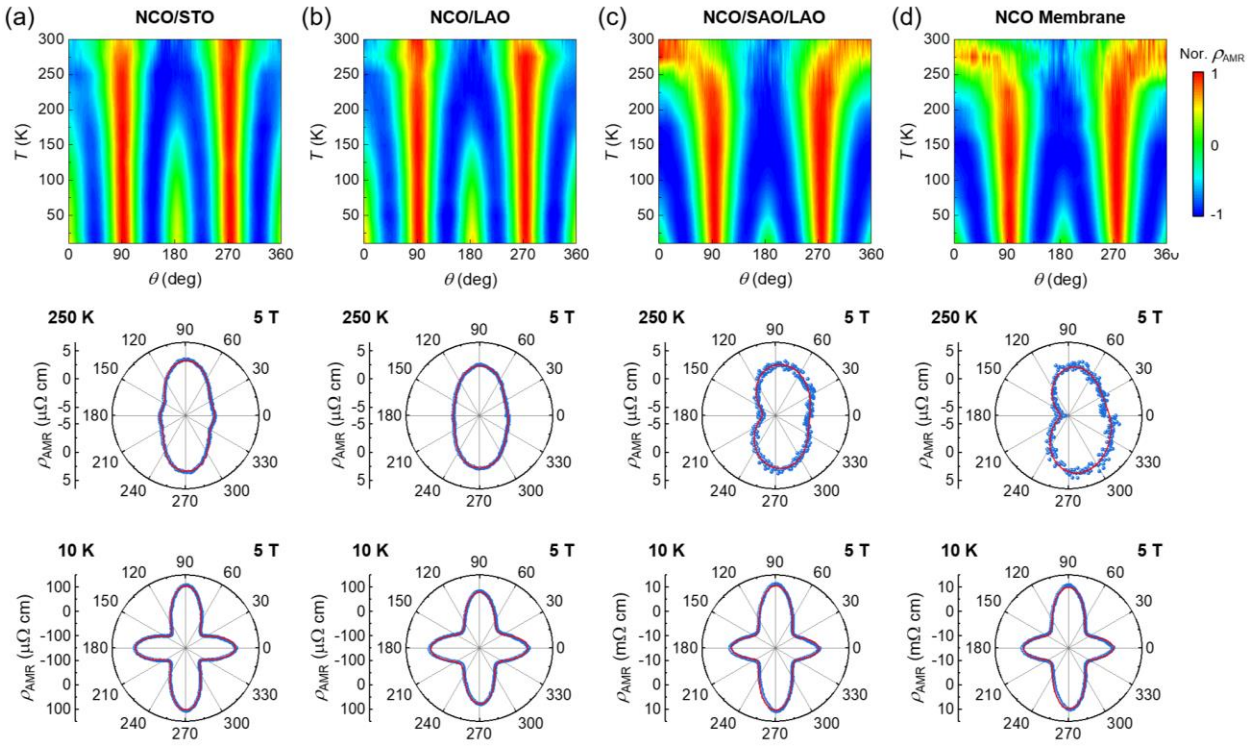

Figure 5. Angular-dependence of in-plane AMR at 5 T. (a-d) Contour plots of normalized ρ_{AMR} vs θ and T (top), and polar plots of ρ_{AMR} vs θ at 250 K (middle) and 10 K (bottom) with fits to Equation 2 (solid lines). (a) NCO/STO. (b) NCO/LAO. (c) NCO/SAO/LAO. (d) NCO membrane.

Similar temperature dependence of ρ_{AMR} has been observed in $NiCo_2O_4$ on $LaAlO_3$ (Figure 5b). For $NiCo_2O_4$ on $Sr_3Al_2O_6$ buffered $LaAlO_3$, ρ_{AMR} exhibits a one-fold oscillation at 300 K (Figure 5c and SI Figure S12), $\rho_{\mathrm{AMR}} = \Delta\rho_{\mathrm{ARM}} \cos\theta$, which is likely dominated by the enhanced MR[53] due to strong spin fluctuation as the sample is approaching T_C. The sample gradually recovers the two-fold symmetric AMR below 250 K, which transitions to the four-fold symmetry below 150 K (SI Figure S12). It is important to note that ρ_{AMR} of the $NiCo_2O_4$ membrane exhibits almost identical field and temperature dependences (Figure 5d and SI Figure S12) to those of the unsuspended NCO/SAO film, suggesting the magnetic anisotropy is not altered by the water etching process. The similar $\rho(T)$, AHE, and AMR behaviors for $NiCo_2O_4$ film on SAO/LAO and $NiCo_2O_4$ membrane collectively demonstrate that the suspension process does not introduce additional defects to the sample.

Figure 6 shows the temperature dependence of C_2 and C_4 amplitude and their ratio C_4/C_2 for the $NiCo_2O_4$ films and membrane, where C_2 and C_4 are determined from the FFT analysis of $\rho_{AMR}(\theta)$ at 5 T (SI Figure S13). For all samples, C_2 and C_4 increase monotonically with decreasing temperature (Figure 6a-b). The temperature dependence of C_2 and C_4 can be well correlated with sample resistivity (Figure 2a) and can be characterized into three groups. For $NiCo_2O_4$ on $MgAl_2O_4$, the small C_2, its weak temperature dependence, and the absence of C_4 is consistent with its metallic nature and strong PMA. NCO/STO and NCO/LAO exhibit similar $\rho(T)$ and similar magnitude of C_2 and C_4 coefficients. NCO/SAO and $NiCo_2O_4$ membrane exhibit substantially higher resistivity. Their C_2 and C_4 coefficients are lower at 300 K and increase rapidly with decreasing temperature, becoming about two orders of magnitude higher than those in NCO/STO and NCO/LAO at 10 K.

Previous studies have suggested that the two-fold and four-fold symmetric AMR can be attributed to small-polaron scattering and anti-phase boundaries,[51-52] respectively, which naturally explain the high C_2 and C_4 values in more insulating samples. This scenario is further supported by two observations: 1) NCO/STO and NCO/LAO exhibit highly consistent AMR despite the large difference in substrate imposed strain; 2) NCO/SAO/LAO exhibits significantly higher AMR than that of NCO/LAO despite the same substrates, which can be attributed to the higher density structural disorders due to the incompatible lattice structure of the $Sr_3Al_2O_6$ buffer layer. $NiCo_2O_4$ membrane shows almost identical C_2 and C_4 to those of unsuspended NCO/SAO film, confirming that the strain and disorder levels are sustained after water etching.

An important observation is the crossover of the temperature dependence of $C_{2,4}$ amplitudes for $NiCo_2O_4$ on $SrTiO_3$ and $LaAlO_3$ with respect to those of NCO/SAO and $NiCo_2O_4$ membranes. At room temperature, the $C_{2,4}$ values for $NiCo_2O_4$ on $SrTiO_3$ and $LaAlO_3$ are higher, despite the smaller disorder contribution to transport, as deduced from $\sigma(T)$ (Figure 2 and Figure S8). As strain-induced tetragonal crystal field can also yield two-fold and four-fold AMR,[54] we can attribute the high temperature AMR to the dominant contribution of the strain modulation of MCA. This scenario is supported by the fact that the C_2 amplitude at 300 K for $NiCo_2O_4$ on the perovskite substrates is comparable with that for $NiCo_2O_4$ on $MgAl_2O_4$ substrates, which is metallic with low disorder density. In contrast, the high density of unsatisfied bonds between $NiCo_2O_4$ and $Sr_3Al_2O_6$ can facilitate local strain relaxation, resulting in reduced strain contribution to AMR in NCO/SAO and $NiCo_2O_4$ membranes. At low temperatures (below 200-250 K), the $C_{2,4}$ amplitudes for NCO/SAO and $NiCo_2O_4$ membrane increases rapidly with decreasing temperature, surpassing

those for $NiCo_2O_4$ on $SrTiO_3$ and $LaAlO_3$. This is consistent with the substantially enhanced resistivity in these samples (Figure 2a). As the sample tetragonality of these samples are similar (SI Table S1), we conclude that the disorder-induced spin scattering dominates AMR in this regime.

The C_4/C_2 ratio further confirms this scenario (Figure 6c). Above 250 K, all samples show similar C_4/C_2 ratios, which can be attributed to the tetragonal crystal field induced MCA.[54] At low temperatures, the C_4/C_2 ratios in $NiCo_2O_4$ on $SrTiO_3$ and $LaAlO_3$ are much higher than those for NCO/SAO and $NiCo_2O_4$ membrane (Figure 6c), which provides important information about the types of disorders that contribute to AMR in $NiCo_2O_4$. A possible scenario is that the AMR in $NiCo_2O_4$ on perovskite substrates is dominated by large scale structural defects, such as grain boundaries and anti-phase boundaries, that change the local crystal field environment and associated spin-orbit interaction,[55] yielding a stronger presence of C_4 component. In contrast, AMR in NCO/SAO and $NiCo_2O_4$ membrane is dominated by small-polaron hopping far away from the large-scale structural defects.[51-52] It is conceivable that, due to the highly incompatible crystal structure, $NiCo_2O_4$ on $Sr_3Al_2O_6$ possesses a larger density of impurity states at Fermi level, consistent with the $N(E_F)$ deduced from the 3D variable range hopping model (SI Table S2).

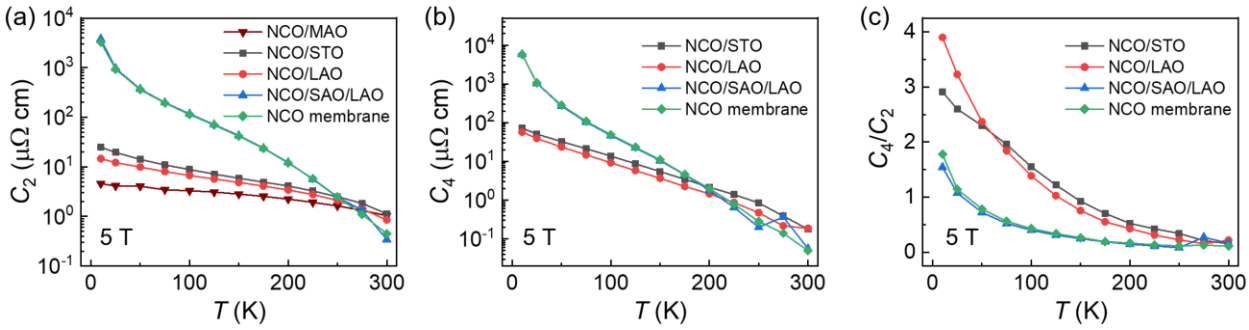

Figure 6. Comparison of C_2 and C_4 components of AMR at 5 T in $NiCo_2O_4$ films and membrane. (a) C_2 vs T. (b) C_4 vs T. (c) C_4/C_2 vs T.

Figure 7 shows the magnetic field dependence of $\rho_{AMR}(\theta)$ at 10 K. At high fields, the Zeeman energy dominates with $\theta \approx \varphi$, and $\rho_{AMR}(\theta)$ does not exhibit pronounced hysteresis. With decreasing magnetic field, the MCA energy becomes increasingly important, and hysteresis behaviors emerge as the magnetization deviates from the magnetic field direction. $NiCo_2O_4$ on $MgAl_2O_4$ exhibits hysteresis-free, two-fold sinusoidal behavior for the entire field and temperature ranges investigated (Figure 4 and SI Figure S11) due to the strong PMA. In contrast, $\rho_{AMR}(\theta)$ for

the insulating $NiCo_2O_4$ samples exhibit clear switching hysteresis as the magnetic field is reduced to below 3 T (Figure 7a-d), clearly illustrating the effect of modified MCA. As the magnetic field is further reduced to 0.5 T, $\rho_{AMR}(\theta)$ clearly deviates from Equation 2, as a one-fold component starts to emerge. At 0.05 T, the AMR exhibits one-fold symmetry similar to those observed at 300 K, showing the dominating contribution of MR due to suppressed spin scattering. Similar one-fold sinusoidal behavior at low magnetic fields has been observed in manganites (La,Ca)MnO_3[53] and (La,Sr)MnO_3[56].

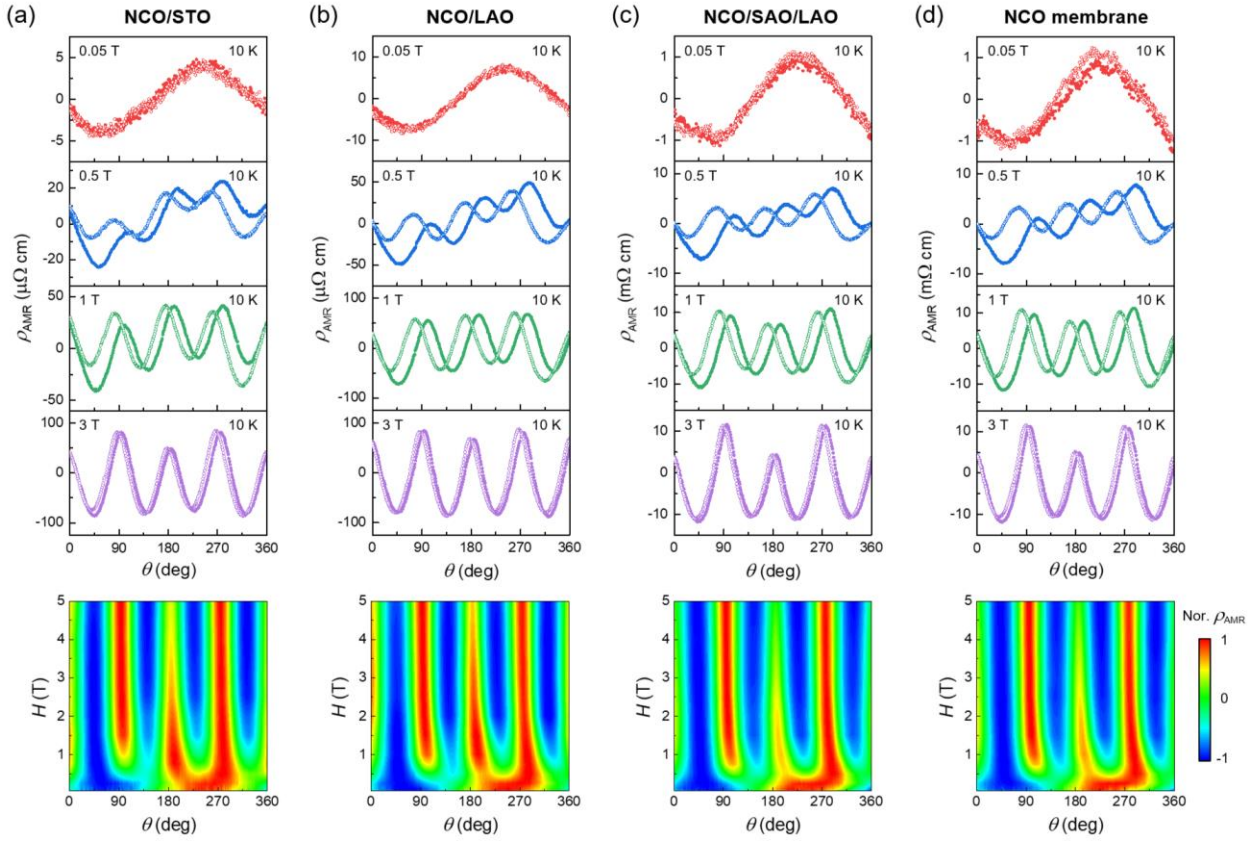

Figure 7. Angular-dependence of in-plane AMR at 10 K and different fields (0.05 T-3 T). ρ_{AMR} vs θ for (a) NCO/STO, (b) NCO/LAO, (c) NCO/SAO/LAO, and (d) NCO membrane (top) and the corresponding contour plots of normalized ρ_{AMR} for the forward-sweeping branch (bottom).

DISCUSSION

Our study reveals important information for engineering $NiCo_2O_4$, one of few conductive magnetic spinels, for integration with other functional oxides and designing room temperature flexible applications. It is worth noting that even though $NiCo_2O_4$ deposited on perovskite substrates and $NiCo_2O_4$ membranes exhibit insulating temperature dependence of resistance, they

remain highly conductive at room temperature. The conductivity varies from 100 to 300 $\Omega^{-1}cm^{-1}$ at 300 K, well exceeding those of magnetic spinel insulators, and is comparable to widely studied conductive magnetic oxides, such as magnetite[57] and (La,Sr)MnO_3[58] thin films of similar thickness. This is because the activation energy for these samples (4.3-8.6 meV) is well below the thermal energy at 300 K, so room temperature conduction is dominated by disorder induced hopping (nearest-neighbor hopping).

The superb transport properties and above room temperature T_C make the disordered $NiCo_2O_4$ films and membrane promising candidates for developing high temperature magnetic sensing and spintronic applications. AMR and associated planar Hall effect can be utilized to develop magnetic sensors and nonvolatile memories.[48, 59] The emergence of the four-fold AMR may facilitate sensing of magnetic field switching and lead to multi-state resistance switching for data storage. Another intriguing opportunity is to use $NiCo_2O_4$ membranes to design high frequency flexible applications. A previous study of $NiCo_2O_4$ has shown via time-resolved magneto-optical Kerr effect microscopy that epitaxial $NiCo_2O_4$ thin films exhibit ultrafast demagnetization with a characteristic time scale of ~0.4 ps.[8] Future studies of the high-frequency properties of $NiCo_2O_4$ membranes, such as magnetic damping via ferromagnetic resonance,[60] are critical for assessing its potential for designing GHz to THz spintronic applications.

CONCLUSIONS

In conclusion, we report the collective effects of epitaxial strain and defects in determining the metallicity, T_C, and AMR in $NiCo_2O_4$ thin films and suspended $NiCo_2O_4$ membranes. $NiCo_2O_4$ films on lattice compatible $MgAl_2O_4$ substrates exhibit high conductivity, band-intrinsic linear MR, and two-fold sinusoidal in-plane AMR with weak temperature dependence. For $NiCo_2O_4$ deposited on perovskite substrates, the high density of defect states and strain relaxation lead to insulating behaviors, large MR, enhanced AMR, and an additional four-fold AMR component at low temperatures. The freestanding $NiCo_2O_4$ membranes display almost identical hopping transport and magnetotransport properties compared with the unsuspended $NiCo_2O_4$ thin films, suggesting the sustained strain and disorder levels. Our study provides important material parameters for designing $NiCo_2O_4$ thin film and membrane-based magnetic sensors and spintronic devices, offering a viable route to integrating magnetic spinels with the rich functionalities of perovskite oxides[22] and designing flexible applications.

METHODS

Sample Preparation. Epitaxial 30 nm $NiCo_2O_4$ thin films were deposited on different substrates of (001) $MgAl_2O_4$, $SrTiO_3$, $LaAlO_3$, and 10 nm $Sr_3Al_2O_6$ buffered (001) $LaAlO_3$ substrate using off-axis radio frequency magnetron sputtering. The $NiCo_2O_4$ layer was deposited at 320 °C with 100 mTorr processing gas ($Ar:O_2$ = 1:1). The $Sr_3Al_2O_6$ layer was deposited at 700 °C with 10 mTorr processing gas ($Ar:O_2$ = 1:8). To achieve the freestanding $NiCo_2O_4$ membranes, the NCO/SAO/LAO samples were immersed into de-ionized water at room-temperature for about 8 hours to dissolve the $Sr_3Al_2O_6$ buffer layer. The NCO/LAO samples were then taken out and dried on the heating plate at 50 °C for 20 min, with the entire NCO membrane laid on the $LaAlO_3$ substrate.

Sample Characterization. XRD and reciprocal space mapping measurements were performed using Rigaku SmartLab Diffractometer (3kW Cu Kα source, Ge(220)×2 monochromator and analyzer). The sample surface morphology was characterized using a Bruker Multimode 8 AFM. The magnetization characterizations were performed using the Superconducting Quantum Interference Device (SQUID) magnetometry in a Quantum Design Magnetic Properties Measurement System (MPMS). We extracted the magnetization of $NiCo_2O_4$ samples by subtracting the diamagnetic background signals from the substrate.

For the TEM measurements, we transferred 28 nm $NiCo_2O_4$ membranes on TEM grids with 500×500 μm size and 20 nm nonporous Silicon Nitride single window (SimPore Precision Membrane Technologies^{TM}). The STEM images were obtained with a JEOL ARM 200CF equipped with a cold-field emission source and two aberration correctors (probe and image) at 200kV electron beam. The collection angle for the HAADF-STEM imaging varies from 68 mrad to 280 mrad. The probe size was 6C and 30 μm size aperture was used. The raw STEM images were band-pass filtered (HREM-Filters Lite, HREM Research Inc., Japan). The EELS data in Figure 1 and SI Figure S6 were measured under 200kV with JEOL 200CF. The dispersion was 0.18 eV/Ch and the acquisition time was 0.24 -0.28 sec per pixel. The energy resolution was ~0.72 eV and the convergence angle and the collection semi-angle were 7.52 mrad and 3.045 mrad, respectively. The EELS data in SI Figure S7 was acquired with dispersion of 0.45 eV/Ch and the acquisition time of 0.01 sec per pixel. The energy resolution was 1.5 eV and the convergence and collection semi-angle were 23.0 mrad and 11.85 mrad, respectively.

Device Fabrication and Magnetotransport Measurements. The van der Pauw and Hall bar geometry were employed to measure the out-of-plane and in-plane magnetotransport properties, respectively. For in-plane AMR measurements, the current was applied along the [100] orientation. The magnetotransport measurements were performed using a Quantum Design Physical Property Measurement System (PPMS) equipped with a sample rotator combined with external Keithley 2400 SourceMeter at the temperature range of 2-350 K and magnetic fields up to 5 T.

ASSOCIATED CONTENT

Supporting Information

Section 1: Structural and surface characterizations of $NiCo_2O_4$ thin films and membranes. Section 2: Suspension of $NiCo_2O_4$ membranes. Section 3: TEM and EELS studies of $NiCo_2O_4$ membranes. Section 4: Temperature dependence of conductivity. Section 5: Anomalous Hall effect in $NiCo_2O_4/MgAl_2O_4$ thin film. Section 6: Magnetic characterizations of $NiCo_2O_4$ thin films and membranes. Section 7: Coherent rotation model for two-fold sinusoidal AMR. Section 8: In-plane AMR in $NiCo_2O_4$ thin films and membranes.

Notes

The authors declare no competing financial interest.

ACKNOWLEDGEMENTS

This work was supported by the National Science Foundation through EPSCoR RII Track-1: Emergent Quantum Materials and Technologies (EQUATE), Award OIA-2044049 (synthesis and characterization of $NiCo_2O_4$ thin films) and the U.S. Department of Energy (DOE), Office of Science, Basic Energy Sciences (BES), under Award No. DE-SC0026103 (synthesis and characterization of $NiCo_2O_4$ membranes). The electron microscopy work at the Brookhaven National Laboratory was supported by the U.S. Department of Energy (DOE), Basic Energy Sciences, Materials Science and Engineering Division, under Contract DESC0012704. This research used electron microscopy resources of the Center for Functional Nanomaterials (CFN), which is a U.S. DOE Office of Science User Facility, at Brookhaven National Laboratory under Contract DESC0012704. The research was performed in part in the Nebraska Nanoscale Facility:

National Nanotechnology Coordinated Infrastructure and the Nebraska Center for Materials and Nanoscience, which are supported by the National Science Foundation under Award ECCS: 2025298, and the Nebraska Research Initiative.

REFERENCES

1. Inomata, K.; Ikeda, N.; Tezuka, N.; Goto, R.; Sugimoto, S.; Wojcik, M.; Jedryka, E., Highly spin-polarized materials and devices for spintronics. *Sci. Technol. Adv. Mater.* **2008,** *9* (1), 014101.
2. Zhao, Q.; Yan, Z. H.; Chen, C. C.; Chen, J., Spinels: Controlled Preparation, Oxygen Reduction/Evolution Reaction Application, and Beyond. *Chem. Rev.* **2017,** *117* (15), 10121-10211.
3. Xu, X.; Mellinger, C.; Cheng, Z. G.; Chen, X.; Hong, X., Epitaxial $NiCo_2O_4$ film as an emergent spintronic material: Magnetism and transport properties. *Journal of Applied Physics* **2022,** *132* (2), 020901.
4. Silwal, P.; Miao, L.; Stern, I.; Zhou, X.; Hu, J.; Ho Kim, D., Metal insulator transition with ferrimagnetic order in epitaxial thin films of spinel $NiCo_2O_4$. *Applied Physics Letters* **2012,** *100* (3), 032102.
5. Chen, X.; Zhang, X.; Han, M. G.; Zhang, L.; Zhu, Y.; Xu, X.; Hong, X., Magnetotransport Anomaly in Room‐Temperature Ferrimagnetic $NiCo_2O_4$ Thin Films. *Advanced Materials* **2019,** *31* (4), 1805260.
6. Chen, X.; Wu, Q.; Zhang, L.; Hao, Y.; Han, M.-G.; Zhu, Y.; Hong, X., Anomalous Hall effect and perpendicular magnetic anisotropy in ultrathin ferrimagnetic $NiCo_2O_4$ films. *Applied Physics Letters* **2022,** *120* (24), 242401.
7. Shen, Y.; Kan, D.; Lin, I.-C.; Chu, M.-W.; Suzuki, I.; Shimakawa, Y., Perpendicular magnetic tunnel junctions based on half-metallic $NiCo_2O_4$. *Applied Physics Letters* **2020,** *117* (4), 042408.
8. Takahashi, R.; Tani, Y.; Abe, H.; Yamasaki, M.; Suzuki, I.; Kan, D.; Shimakawa, Y.; Wadati, H., Ultrafast demagnetization in $NiCo_2O_4$ thin films probed by time-resolved microscopy. *Applied Physics Letters* **2021,** *119* (10), 102404.
9. Mellinger, C.; Waybright, J.; Zhang, X.; Schmidt, C.; Xu, X., Perpendicular magnetic anisotropy in conducting $NiCo_2O_4$ films from spin-lattice coupling. *Physical Review B* **2020,** *101* (1), 014413.
10. Silwal, P.; Miao, L.; Hu, J.; Spinu, L.; Ho Kim, D.; Talbayev, D., Thickness dependent structural, magnetic, and electronic properties of the epitaxial films of transparent conducting oxide $NiCo_2O_4$. *Journal of Applied Physics* **2013,** *114* (10), 103704.
11. Koizumi, H.; Yamasaki, Y.; Yanagihara, H., Quadrupole anomalous Hall effect in magnetically induced electron nematic state. *Nature Communications* **2023,** *14* (1), 8074.

12. Suzuki, Y., Epitaxial spinel ferrite thin films. *Ann. Rev. Mater. Res.* **2001,** *31*, 265-289.

13. Dubal, D. P.; Gomez-Romero, P.; Sankapal, B. R.; Holze, R., Nickel cobaltite as an emerging material for supercapacitors: an overview. *Nano Energy* **2015,** *11*, 377-399.

14. Sasmal, A.; Nayak, A. K., Morphology-dependent solvothermal synthesis of spinel $NiCo_2O_4$ nanostructures for enhanced energy storage device application. *Journal of Energy Storage* **2023,** *58*, 106342.

15. Cui, B.; Lin, H.; Li, J. B.; Li, X.; Yang, J.; Tao, J., Core–ring structured $NiCo_2O_4$ nanoplatelets: synthesis, characterization, and electrocatalytic applications. *Advanced Functional Materials* **2008,** *18* (9), 1440-1447.

16. Li, Y.; Hasin, P.; Wu, Y., $Ni_xCo_{3-x}O_4$ nanowire arrays for electrocatalytic oxygen evolution. *Advanced materials* **2010,** *22* (17), 1926-1929.

17. Prathap, M. A.; Srivastava, R., Synthesis of $NiCo_2O_4$ and its application in the electrocatalytic oxidation of methanol. *Nano Energy* **2013,** *2* (5), 1046-1053.

18. Li, P.; Xia, C.; Li, J.; Zhu, Z.; Wen, Y.; Zhang, Q.; Zhang, J.; Peng, Y.; Alshareef, H. N.; Zhang, X., Spin filtering in epitaxial spinel films with nanoscale phase separation. *ACS nano* **2017,** *11* (5), 5011-5019.

19. Koizumi, H.; Yamasaki, Y., Altermagnetism in epitaxial $NiCo_2O_4$ thin films via higher-order magnetic anisotropy. *Journal of Physics D: Applied Physics* **2025,** *58* (25), 253002.

20. Lu, D.; Baek, D. J.; Hong, S. S.; Kourkoutis, L. F.; Hikita, Y.; Hwang, Harold Y., Synthesis of freestanding single-crystal perovskite films and heterostructures by etching of sacrificial water-soluble layers. *Nature Materials* **2016,** *15* (12), 1255-1260.

21. Pesquera, D.; Fernandez, A.; Khestanova, E.; Martin, L. W., Freestanding complex-oxide membranes. *J Phys Condens Matter* **2022,** *34* (38), 383001.

22. Hao, Y. F.; Li, T. L.; Hong, X., Interface phenomena and emerging functionalities in ferroelectric oxide based heterostructures. *Chemical Communications* **2025,** *61* (26), 4924-4950.

23. Bakaul, S. R.; Kim, J.; Hong, S.; Cherukara, M. J.; Zhou, T.; Stan, L.; Serrao, C. R.; Salahuddin, S.; Petford-Long, A. K.; Fong, D. D.; Holt, M. V., Ferroelectric Domain Wall Motion in Freestanding Single-Crystal Complex Oxide Thin Film. *Adv Mater* **2020,** *32* (4), 1907036.

24. Wu, Q.; Wang, K.; Simpson, A.; Hao, Y.; Wang, J.; Li, D.; Hong, X., Electrode Effect on Ferroelectricity in Free-Standing Membranes of $PbZr_{0.2}Ti_{0.8}O_3$. *ACS Nanoscience Au* **2023,** *3* (6), 482-490.

25. Xu, R.; Huang, J.; Barnard, E. S.; Hong, S. S.; Singh, P.; Wong, E. K.; Jansen, T.; Harbola, V.; Xiao, J.; Wang, B. Y., Strain-induced room-temperature ferroelectricity in $SrTiO_3$ membranes. *Nature communications* **2020,** *11* (1), 3141.

26. Peng, W.; Park, S. Y.; Roh, C. J.; Mun, J.; Ju, H.; Kim, J.; Ko, E. K.; Liang, Z.; Hahn, S.; Zhang, J.; Sanchez, A. M.; Walker, D.; Hindmarsh, S.; Si, L.; Jo, Y. J.; Jo, Y.; Kim, T. H.; Kim, C.; Wang, L.; Kim, M.; Lee, J. S.; Noh, T. W.; Lee, D., Flexoelectric polarizing and control of a ferromagnetic metal. *Nature Physics* **2024,** *20* (3), 450-455.

27. Sánchez-Santolino, G.; Rouco, V.; Puebla, S.; Aramberri, H.; Zamora, V.; Cabero, M.; Cuellar, F.; Munuera, C.; Mompean, F.; García-Hernández, M., A 2D ferroelectric vortex pattern in twisted $BaTiO_3$ freestanding layers. *Nature* **2024,** *626* (7999), 529-534.

28. Li, Y.; Xiang, C.; Chiabrera, F. M.; Yun, S.; Zhang, H. W.; Kelly, D. J.; Dahm, R. T.; Kirchert, C. K. R.; Le Cozannet, T. E.; Trier, F.; Christensen, D.; Booth, T. J.; Simonsen, S. B.; Kadkhodazadeh, S.; Jespersen, T. S.; Pryds, N., Stacking and Twisting of Freestanding Complex Oxide Thin Films. *Advanced Materials* **2022,** *34* (38), 2203187.

29. Puebla, S.; Pucher, T.; Rouco, V.; Sanchez-Santolino, G.; Xie, Y.; Zamora, V.; Cuellar, F. A.; Mompean, F. J.; Leon, C.; Island, J. O.; Garcia-Hernandez, M.; Santamaria, J.; Munuera, C.; Castellanos-Gomez, A., Combining Freestanding Ferroelectric Perovskite Oxides with Two-Dimensional Semiconductors for High Performance Transistors. *Nano Letters* **2022,** *22* (18), 7457-7466.

30. Lu, C.; Li, M.; Gao, L.; Zhang, Q.; Zhu, M.; Lyu, X.; Wang, Y.; Liu, J.; Liu, P.; Wang, L., Freestanding crystalline β-Ga_2O_3 flexible membrane obtained via lattice epitaxy engineering for high-performance optoelectronic device. *ACS nano* **2024,** *18* (7), 5374-5382.

31. Lu, D.; Crossley, S.; Xu, R.; Hikita, Y.; Hwang, H. Y., Freestanding oxide ferroelectric tunnel junction memories transferred onto silicon. *Nano Letters* **2019,** *19* (6), 3999-4003.

32. Li, R.; Xu, Y.; Song, J.; Wang, P.; Li, C.; Wu, D., Preparation and characterization of a flexible ferroelectric tunnel junction. *Applied Physics Letters* **2020,** *116* (22), 222904.

33. Yao, M.; Li, Y.; Tian, B.; Mao, Q.; Dong, G.; Cheng, Y.; Hou, W.; Zhao, Y.; Wang, T.; Zhao, Y.; Jiang, Z.; Liu, M.; Zhou, Z., Freestanding single-crystal $Ni_{0.5}Zn_{0.5}Fe_2O_4$ ferrite membranes with controllable enhanced magnetic properties for flexible RF/microwave applications. *Journal of Materials Chemistry C* **2020,** *8* (47), 17099-17106.

34. Salles, P.; Guzmán, R.; Zanders, D.; Quintana, A.; Fina, I.; Sánchez, F.; Zhou, W.; Devi, A.; Coll, M., Bendable Polycrystalline and Magnetic $CoFe_2O_4$ Membranes by Chemical Methods. *ACS Applied Materials & Interfaces* **2022,** *14* (10), 12845-12854.

35. Zhang, J. F.; Lin, T.; Wang, A.; Wang, X. C.; He, Q. Y.; Ye, H.; Lu, J. D.; Wang, Q.; Liang, Z. G.; Jin, F.; Chen, S. R.; Fan, M. H.; Guo, E. J.; Zhang, Q. H.; Gu, L.; Luo, Z. L.; Si, L.; Wu, W. B.; Wang, L. F., Super-tetragonal $Sr_4Al_2O_7$ as a sacrificial layer for high-integrity freestanding oxide membranes. *Science* **2024,** *383* (6681), 388-394.

36. Xue, M.; Chen, X.; Ding, S.; Liang, Z.; Peng, Y.; Li, X.; Zha, L.; Yang, W.; Han, J.; Liu, S.; Du, H.; Wang, C.; Yang, J., Transport Anomaly in Perpendicular Magnetic Anisotropic $NiCo_2O_4$ Thin Films with Column-like Phase Separation. *ACS Applied Electronic Materials* **2020,** *2* (12), 3964-3970.

37. Zhen, C.; Zhang, X.; Wei, W.; Guo, W.; Pant, A.; Xu, X.; Shen, J.; Ma, L.; Hou, D., Nanostructural origin of semiconductivity and large magnetoresistance in epitaxial $NiCo_2O_4/Al_2O_3$ thin films. *Journal of Physics D: Applied Physics* **2018,** *51* (14), 145308.

38. Cabo, M.; Pellicer, E.; Rossinyol, E.; Castell, O.; Suriñach, S.; Baró, M. D., Mesoporous $NiCo_2O_4$ Spinel: Influence of Calcination Temperature over Phase Purity and Thermal Stability. *Crystal Growth & Design* **2009,** *9* (11), 4814-4821.

39. Bitla, Y.; Chin, Y.-Y.; Lin, J.-C.; Van, C. N.; Liu, R.; Zhu, Y.; Liu, H.-J.; Zhan, Q.; Lin, H.-J.; Chen, C.-T., Origin of metallic behavior in $NiCo_2O_4$ ferrimagnet. *Scientific reports* **2015,** *5* (1), 15201.

40. Lv, H.; Huang, X. C.; Zhang, K. H. L.; Bierwagen, O.; Ramsteiner, M., Underlying mechanisms and tunability of the anomalous Hall effect in $NiCo_2O_4$ films with robust perpendicular magnetic anisotropy. *Advanced Science* **2023,** *10* (28), 2302956.

41. Hu, L.; Wu, L.; Liao, M.; Hu, X.; Fang, X., Electrical transport properties of large, individual $NiCo_2O_4$ nanoplates. *Advanced Functional Materials* **2012,** *22* (5), 998-1004.

42. Zhang, L.; Chen, X. G.; Gardner, H. J.; Koten, M. A.; Shield, J. E.; Hong, X., Effect of strain on ferroelectric field effect in strongly correlated oxide $Sm_{0.5}Nd_{0.5}NiO_3$. *Applied Physics Letters* **2015,** *107* (15), 152906.

43. Zhang, L.; Jiang, X.; Xu, X.; Hong, X., Abrupt enhancement of spin–orbit scattering time in ultrathin semimetallic $SrIrO_3$ close to the metal–insulator transition. *APL Materials* **2020,** *8* (5), 051108.

44. Xiao, C.; Chen, H.; Gao, Y.; Xiao, D.; MacDonald, A. H.; Niu, Q., Linear magnetoresistance induced by intra-scattering semiclassics of Bloch electrons. *Physical Review B* **2020,** *101* (20), 201410.

45. Li, P.; Xia, C.; Zheng, D.; Wang, P.; Jin, C.; Bai, H., Observation of large low‐field magnetoresistance in spinel cobaltite: A new half‐metal. *physica status solidi (RRL)–Rapid Research Letters* **2016,** *10* (2), 190-196.

46. Koizumi, H.; Suzuki, I.; Kan, D.; Inoue, J.-i.; Wakabayashi, Y.; Shimakawa, Y.; Yanagihara, H., Spin reorientation in tetragonally distorted spinel oxide $NiCo_2O_4$ epitaxial films. *Physical Review B* **2021,** *104* (1), 014422.

47. Margulies, D. T.; Parker, F. T.; Spada, F. E.; Goldman, R. S.; Li, J.; Sinclair, R.; Berkowitz, A. E., Anomalous moment and anisotropy behavior in Fe_3O_4 films. *Physical Review B* **1996,** *53* (14), 9175-9187.

48. Li, T.; Zhang, L.; Hong, X., Anisotropic magnetoresistance and planar Hall effect in correlated and topological materials. *Journal of Vacuum Science & Technology A* **2022,** *40* (1), 010807.

49. McGuire, T.; Potter, R., Anisotropic magnetoresistance in ferromagnetic 3d alloys. *IEEE Transactions on magnetics* **1975,** *11* (4), 1018-1038.

50. Birss, R. R., *Symmetry and magnetism*; North‐Holland: Amsterdam, **1964**.

51. Li, P.; Jin, C.; Jiang, E.; Bai, H., Origin of the twofold and fourfold symmetric anisotropic magnetoresistance in epitaxial Fe_3O_4 films. *Journal of Applied Physics* **2010,** *108* (9), 093921.

52. Li, P.; Jiang, E.; Bai, H., Fourfold symmetric anisotropic magnetoresistance based on magnetocrystalline anisotropy and antiphase boundaries in reactive sputtered epitaxial Fe_3O_4 films. *Applied Physics Letters* **2010,** *96* (9), 092502.

53. O'Donnell, J.; Onellion, M.; Rzchowski, M.; Eckstein, J.; Bozovic, I., Low-field magnetoresistance in tetragonal $La_{1-x}Ca_xMnO_3$ films. *Physical Review B* **1997,** *55* (9), 5873.

54. Kokado, S.; Tsunoda, M., Twofold and fourfold symmetric anisotropic magnetoresistance effect in a model with crystal field. *Journal of the Physical Society of Japan* **2015,** *84* (9), 094710.

55. Yahagi, Y.; Miura, D.; Sakuma, A., Theoretical Study on Four-fold Symmetric Anisotropic Magnetoresistance Effect in Cubic Single-crystal Ferromagnetic Model. *Journal of the Physical Society of Japan* **2020,** *89* (4), 044714.

56. Zhao, W.; Zhang, D.; Meng, D.; Huang, W.; Feng, L.; Hou, C.; Lu, Y.; Yin, Y.; Li, X., Electric-field-controlled nonvolatile magnetic switching and resistive change in $La_{0.6}Sr_{0.4}MnO_3$/0.7Pb($Mg_{1/3}Nb_{2/3}O_3$-0.3$PbTiO_3$ (011) heterostructure at room temperature. *Applied Physics Letters* **2016,** *109* (26), 263502.

57. Reisinger, D.; Majewski, P.; Opel, M.; Alff, L.; Gross, R., Hall effect, magnetization, and conductivity of Fe_3O_4 epitaxial thin films. *Applied Physics Letters* **2004,** *85* (21), 4980-4982.

58. Yau, J.-B.; Hong, X.; Posadas, A.; Ahn, C. H.; Gao, W.; Altman, E.; Bason, Y.; Klein, L.; Sidorov, M.; Krivokapic, Z., Anisotropic magnetoresistance in colossal magnetoresistive $La_{1-x}Sr_xMnO_3$ thin films. *Journal of Applied Physics* **2007,** *102* (10), 103901.

59. Bason, Y.; Klein, L.; Wang, H. Q.; Hoffman, J.; Hong, X.; Henrich, V. E.; Ahn, C. H., Planar Hall effect in epitaxial thin films of magnetite. *Journal of Applied Physics* **2007,** *101* (9), 09J507.

60. Zheng, X. Y.; Channa, S.; Riddiford, L. J.; Wisser, J. J.; Mahalingam, K.; Bowers, C. T.; McConney, M. E.; N'Diaye, A. T.; Vailionis, A.; Cogulu, E.; Ren, H.; Galazka, Z.; Kent, A. D.; Suzuki, Y., Ultra-thin lithium aluminate spinel ferrite films with perpendicular magnetic anisotropy and low damping. *Nature Communications* **2023,** *14* (1), 4918.

Table of Contents

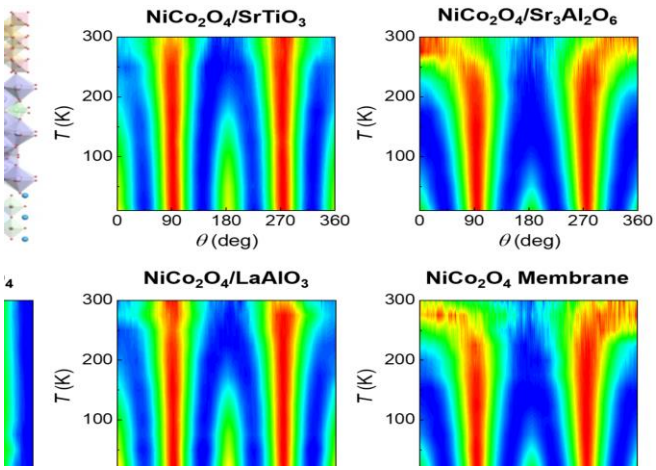

Supporting Information

Strain and Defect-Tailored Magnetotransport in $NiCo_2O_4$ Thin Films and Freestanding Membranes

Qiuchen Wu,[1] Yuanyuan Zhang,[1] Tianlin Li,[1] Myung-Geun Han,[2] Soo-Yoon Hwang,[2,3] Yeon-Seo Nam,[2,3] Si-Young Choi,[3] Yimei Zhu,[2] and Xia Hong[1,*]

[1] Department of Physics and Astronomy & Nebraska Center for Materials and Nanoscience, University of Nebraska–Lincoln, Lincoln, NE 68588-0299, USA

[2] Condensed Matter Physics and Materials Science Department, Brookhaven National Laboratory, Upton, NY 11973-5000, USA

[3] Department of Materials Science and Engineering, Pohang University of Science and Technology (POSTECH), Pohang 37673, Republic of Korea

[*] Author to whom correspondence should be addressed: xia.hong@unl.edu

Contents

1. Structural and Surface Characterizations of $NiCo_2O_4$ Thin Films and Membranes

Epitaxial $NiCo_2O_4$ (NCO) films are deposited on (001) $MgAl_2O_4$ (MAO), $SrTiO_3$ (STO), and $LaAlO_3$ (LAO) substrates as well as $Sr_3Al_2O_6$ (SAO)-buffered LAO using off-axis RF magnetron sputtering. The samples possess smooth surface morphology and high crystallinity, as revealed by atomic force microscopy (AFM) and x-ray diffraction (XRD), respectively. Figures S1a shows the AFM topography image taken on NCO on MAO, which shows a root-mean-square (RMS) roughness of 2 Å. XRD θ-2θ measurement reveals (001) growth of NCO on MAO with the *c*-axis lattice constant of 8.196 Å (Figures S1b). The Laue oscillation around the main Bragg peak (Figure S1b inset) reflects the high sample quality and has been used to deduce the film thickness. Figure S1c shows the AFM image of NCO on STO, which shows an RMS roughness of 3 Å. XRD θ-2θ scan reveals (001) growth with the *c*-axis lattice constant of 8.207 Å (Figure S1d). The characterizations of NCO on LAO and SAO/LAO are shown in Figure 1a in the main text. The RMS roughness of the samples is listed in Table S1.

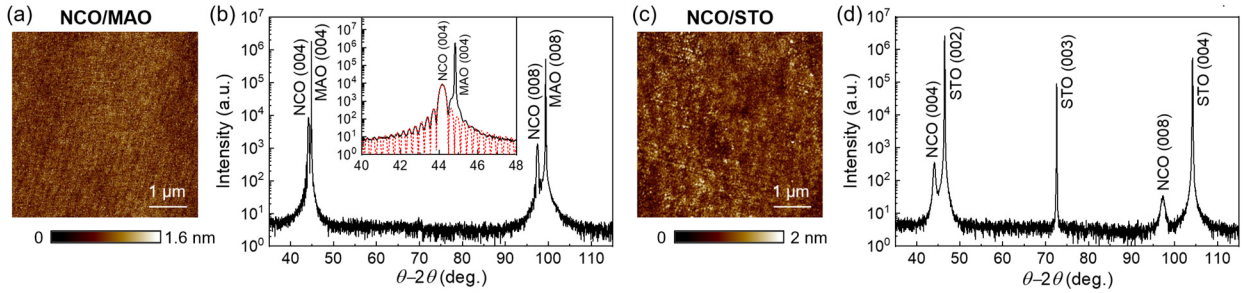

Figure S1. Structural and surface characterizations of 30 nm (001) NCO thin films. (a) AFM topography image and (b) XRD θ-2θ scan taken on NCO on MAO. Inset in (b): expanded view around the (004) peak with a fit to the Laue oscillations of 30 nm thickness. (c) AFM topography image and (d) XRD θ-2θ scan taken on NCO on STO.

Sample	**NCO/MAO**	**NCO/STO**	**NCO/LAO**	**NCO/SAO/LAO**	**NCO membrane**
RMS roughness (Å)	2	3	6	2	6
***a* (Å)**	8.097	8.060	8.116	8.070	8.095
***c* (Å)**	8.195	8.213	8.158	8.183	8.169
c*/*a	1.012	1.019	1.005	1.014	1.009
Rocking curve FWHM	0.09°	1.42°	1.87°	1.59°	1.82°

Table S1. Surface roughness, lattice parameters deduced from RSM, and rocking curve FWHM of 30 nm NCO films on different substrates and NCO membrane.

Figure S2 shows the XRD rocking curves around the (004) peaks taken on the NCO films and freestanding NCO membrane. NCO/MAO shows a small full-width-at-half-maximum (FWHM) value of 0.09°, indicating the high crystallinity of the sample. Other NCO samples show much broader rocking-curve peaks (Table S1), consistent with partial relaxation of epitaxial strain.

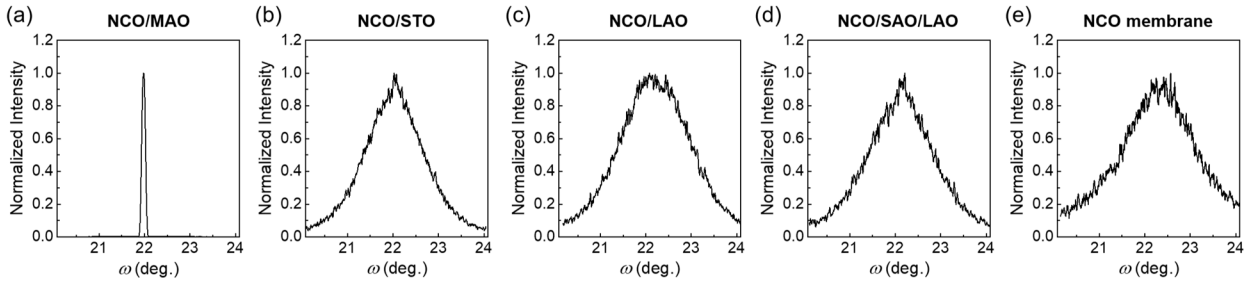

Figure S2. Rocking curves around the (004) peaks for NCO thin films and NCO membrane. (a) NCO/MAO. (b) NCO/STO. (c) NCO/LAO. (d) NCO/SAO/LAO. (e) NCO membrane.

Figure S3 shows the reciprocal space mapping (RSM) of NCO thin films on different substrates and NCO membranes. The NCO film on MAO remains fully strained, while NCO films on the perovskite substrates are partially relaxed. Table S1 summarizes the in-plane and out-of-plane lattice constants deduced from RSM. The out-of-plane lattice constants agree well with those extracted from the XRD measurements. The SAO buffer layer is strain relaxed with an in-plane lattice constant of 15.766 Å. The in-plane lattice constant of NCO membrane slightly increases after water etching of SAO, consistent with the reduced out-of-plane value.

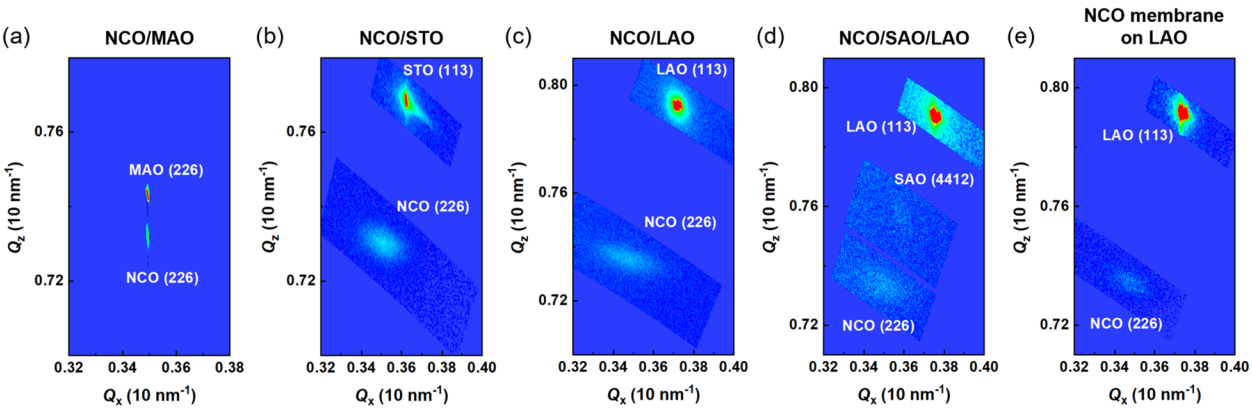

Figure S3. Reciprocal space maps of 30 nm NCO on different substrates and NCO membrane. (a) NCO/MAO. (b) NCO/STO. (c) NCO/LAO. (d) NCO on 10 nm SAO-buffered LAO. (e) NCO membrane laid on LAO after water-etching of SAO.

2. Suspension of $NiCo_2O_4$ Membranes

We immerse 30 nm NCO/10 nm SAO/LAO thin film into the de-ionized water to dissolve the SAO layer. Figure S4a shows the optical images of the sample during the water etching process. The SAO buffer layer begins to dissolve immediately after being immersed into water. Most of the SAO layer has been etched within 10 minutes. After 8 hours, the SAO buffer layer has been fully etched, and the suspended NCO membrane is laid on the LAO substrate (Figure S4b-c). After the sample is taken out of water and dried, the majority area of the suspended NCO membrane recovers to a flat surface with few cracks (Figure S4d-e).

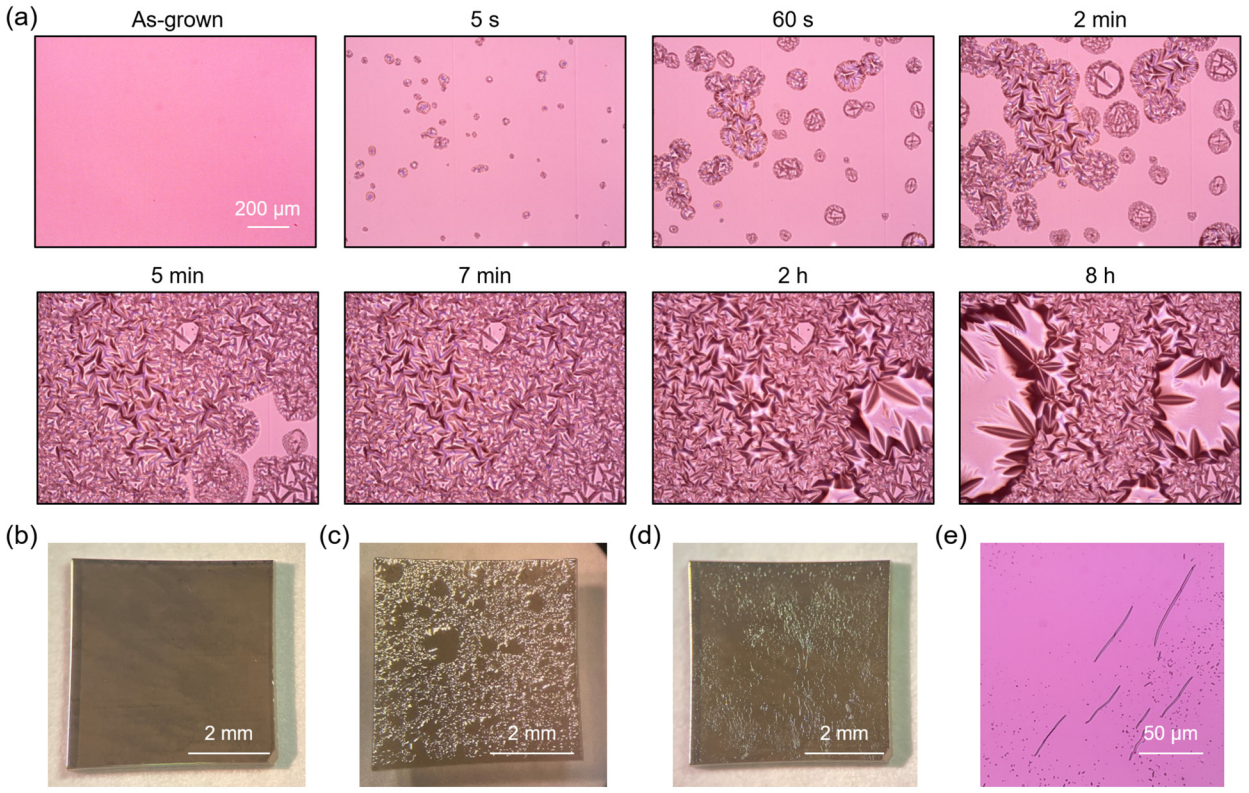

Figure S4. Optical images of NCO/SAO/LAO during water etching. (a) Optical images of a sample in the as-grown state and at different time intervals after being immersed in water. (b-d) Optical images of a 5 mm by 5 mm NCO/SAO/LAO thin film sample in the as-grown state (b), after being immersed in water for 8 hours (c), and being picked up from water and dried (d). (e) A zoomed-in view of (d).

3. TEM and EELS Studies of $NiCo_2O_4$ Membranes

We use Gel-films to pick up and transfer NCO membranes on transmission electron microscopy (TEM) grids for the TEM measurements (Figure S5).

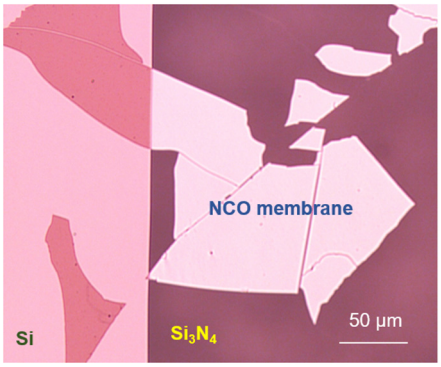

Figure S5. Optical image of NCO membrane flakes transferred on a TEM grid.

Figure S6a-b shows the electron energy loss spectroscopy (EELS) measurements taken in the regions of the high-angle annular dark-field scanning TEM (HAADF-STEM) images shown in Figures 1f and 1h in the main text, respectively. For the imperfect structure of NCO (Figure S6b), the intensity of Co-L peak is much weaker than that of the ideal inverse spinel NCO structure (Figure S6a), supporting the A-site cation deficiency.

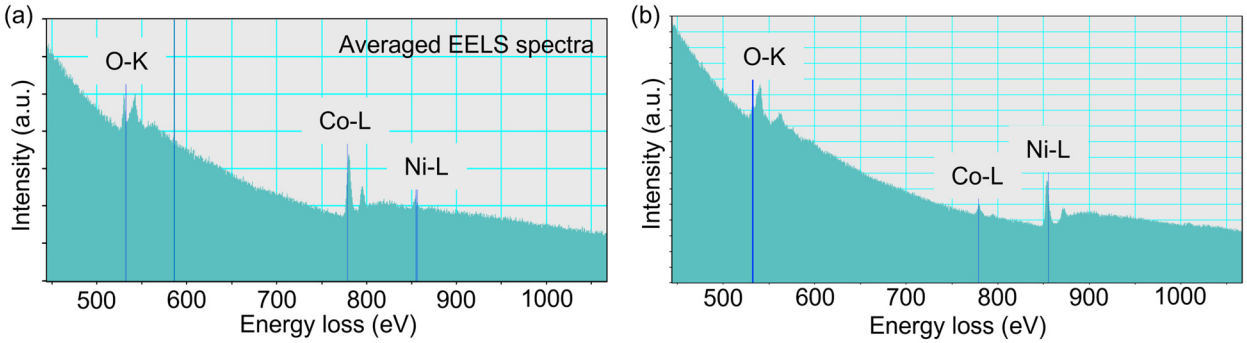

Figure S6. EELS spectra of NCO membrane taken on the regions of HAADF-STEM images shown in Figure 1f (a) and Figure 1h (b) in the main text.

Figure S7a shows the enlarged HAADF-STEM image taken on the NCO membrane that hosts a typical bright patch region. Compared with the ideal inverse spinel (Figure 1e), the fast Fourier transform (FFT) image shows that the (220) diffraction peaks are missing (Figure S7b). Figure S7c shows HAADF-STEM image taken on a region containing many bright patches. For chemical element analysis, we take the corresponding EELS maps (Figure S7d) and EELS spectra (Figure S7e). The results clearly show that the bright patch areas mainly contain Ni ions, with Co ions missing. These regions do not contain Al ions, so we can rule out undissolved $Sr_3Al_2O_6$ buffer layer as the origin.

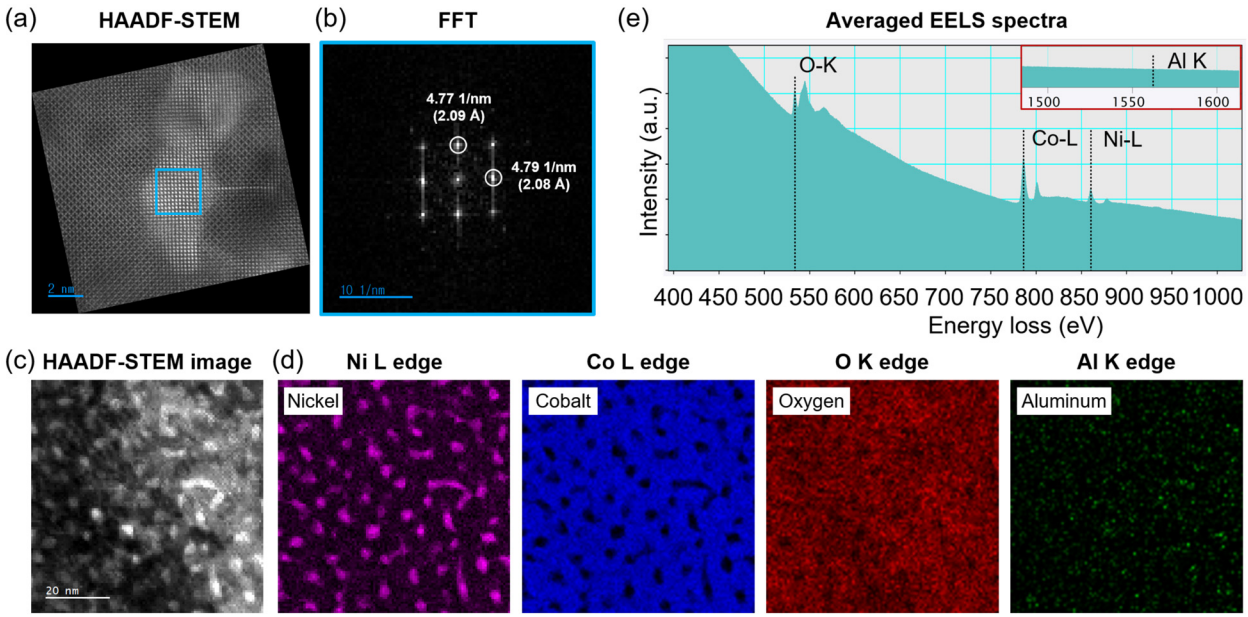

Figure S7. Chemical analysis of the bright regions in NCO membrane. (a) HAADF-STEM image of a region containing a typical bright patch. (b) FFT image from the blue boxed region in (a). (c) HAADF-STEM image of a region hosting lots of bright patch regions, and (d) the corresponding EELS maps for Ni-L, Co-L, O-K, and Al-K edges. (e) Averaged EELS spectra highlighting the Ni-L, Co-L and O-K signals. Inset: Al-K signals.

For HAADF-STEM imaging, atomic columns containing heavier atoms appear brighter because the brightness roughly scales with the atomic number (Z). The bright embedded patch area is thus likely NiO, which has been widely observed in thermally treated NCO thin films[1] and nanostructures[2] as NiO is thermodynamically more stable than NCO.[3] Here, we estimate the total Z-contrast values of NCO and NiO patch regions by multiplying the number of unit cells within a 28 nm thick membrane by the atomic numbers of the atoms in each column. For inverse spinel NCO, assuming the *c*-axis lattice parameter is 8.15 Å, there are about 35 unit cells of NCO in a 28 nm membrane. Each A-site column contains one Co atom (Z = 27), and the total Z-contrast value is ~945. Each B-site column contains one Ni/Co atom (average Z = 27.5) and two O atoms (Z = 8 each), and the total Z-contrast value is ~1523. For NiO, the cubic lattice parameter is 4.18 Å, which yields about 67 unit cells for a 28 nm membrane. Each column contains one Ni atom (Z = 28) and one O atom (Z = 8), resulting in a total Z-contrast value of ~2412. Therefore, the accumulated Z-contrast per column for the NiO patch region is larger than that of either the A-site or B-site columns in NCO, and it appears brighter than the NCO region in the HAADF-STEM image.

4. Temperature Dependence of Conductivity

Figure S8 shows the temperature dependence of conductivity $\sigma(T)$ for the 30 nm NCO/LAO, NCO/SAO/LAO, NCO membrane, and 1.5 unit cell (uc) or ~1.2 nm NCO/MAO. All data can be well described by considering contributions of thermal activation, nearest-neighbor hopping (NNH), and 3D variable range hopping (VRH) (Equation 1 in the main text).

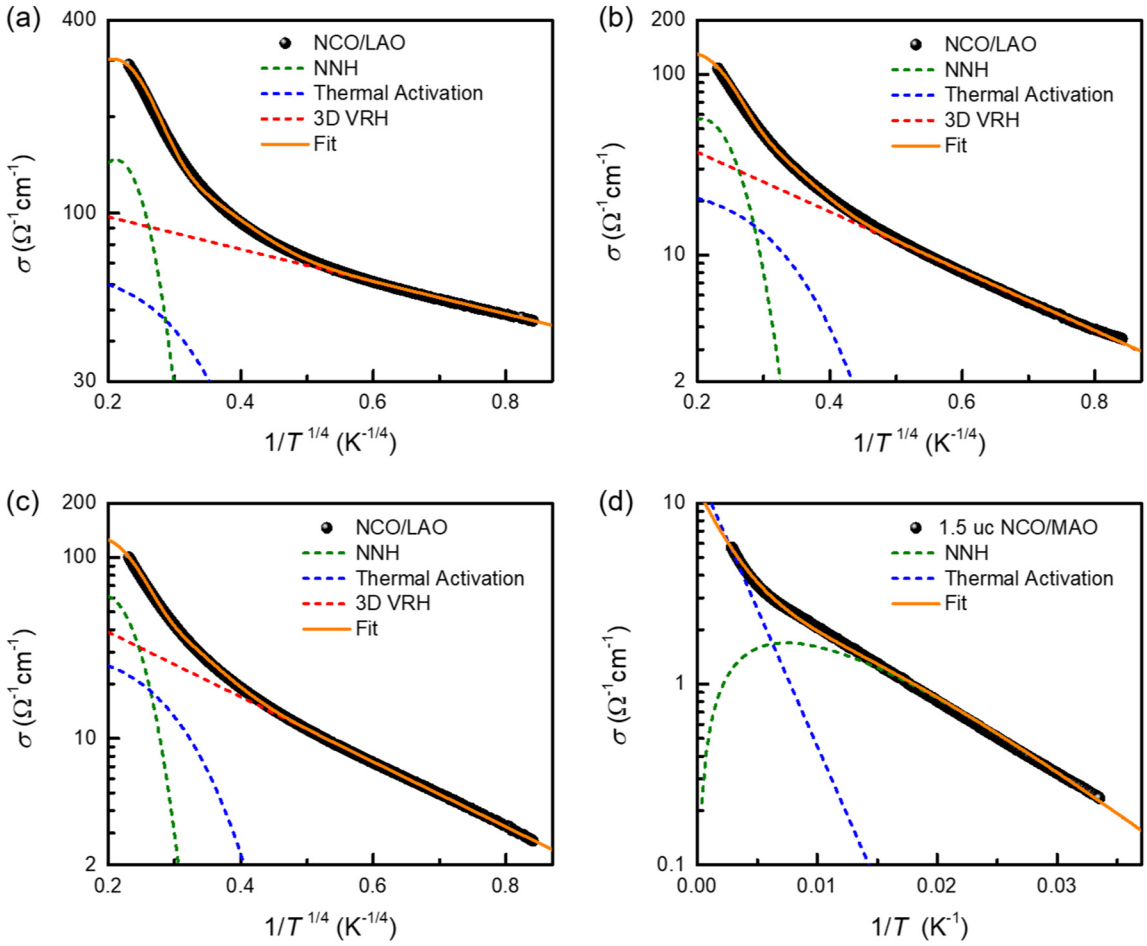

Figure S8. $\sigma(T)$ for (a) 30 nm NCO/LAO, (b) 30 nm NCO/SAO/LAO, (c) 30 nm NCO membrane, and (d) 1.5 uc NCO/MAO with fits considering thermal activation, 3D VRH, and NNH. The individual contributions are also shown.

For the parameters in the 3D VRH model term,[4]

$$\sigma_{\mathrm{VR}} = e^2 a^2 \gamma_{ph} N(E_F)\,, \tag{S1}$$

$$T_{VR} = \frac{18.1}{k_B N(E_F) a^3}\,, \tag{S2}$$

where a is the localization length of the charge carriers, $\gamma_{ph} \sim 2 \times 10^{12} s^{-1}$ is the optical phonon frequency estimated from the Debye temperature of NCO,[5] and $N(E_F)$ is the density of impurity states at the Fermi level.

As shown in Figure S8a-c, for the 30 nm NCO films on LAO and SAO-buffered LAO and the NCO membrane, nearest-neighbor hopping dominates at high temperatures and thermal activation becomes important in the intermediate temperature range. Both contributions diminish quickly at low temperatures, while the nearest-neighbor hopping decays faster. At low temperatures, variable-range hopping dominates. This is in sharp contrast to $\sigma(T)$ of an ultrathin 1.2 nm (1.5 uc) NCO film on MAO, which exhibits a thickness-driven insulating behavior due to the finite size effect.[6] The 1.5 uc NCO on MAO is significantly more resistive, which can be well accounted for by thermal activation at high temperatures followed by NNH at low temperatures.

Sample	σ_0 (Ω^{-1}cm^{-1})	E_A (meV)	c_{NN} (Ω^{-1}cm^{-1}K)	T_{NN} (K)	σ_{VR} (Ω^{-1}cm^{-1})	T_{VR} (K)	a (nm)	$N(E_F)$ (cm^{-3} eV^{-1})
30 nm NCO/STO	50	5.6	1.8×10^5	570	108	4.8	1300	1.3×10^{15}
30 nm NCO/LAO	65	4.3	2.0×10^5	500	123	1.8	3022	2.8×10^{14}
30 nm NCO/SAO/LAO	35	8.2	1.1×10^5	650	80.0	209	40.4	1.0×10^{18}
30 nm NCO membrane	30	8.6	1.2×10^5	715	88.6	291	26.1	2.7×10^{18}
1.5 uc NCO/MAO	12	30.2	6.2×10^4	135				

Table S2. Fitting parameters based on Equation 1 in the main text for NCO films on different substrates and NCO membrane, and the corresponding localization length *a* and density of impurity states at the Fermi level $N(E_F)$ deduced from Equations S1-S2.

Table S2 summarizes the fitting parameters for modeling $\sigma(T)$ based on Equations 1 and S1-S2 (Figures 2b and S8). For the 1.5 uc NCO/MAO, the thermal activation energy is about 30 meV, significantly larger than those of 30 nm NCO thin films grown on perovskite substrates and NCO membranes, which can be attributed to the emergence of a correlation gap at the ultrathin limit.[6] The small T_{NN} and absence of the VRH contribution clearly show the low disorder level in this sample (Table S2). The other types of NCO samples exhibit similar parameters for the thermal activation and nearest neighbor hopping. For the VRH contribution, the NCO/SAO/LAO film and NCO membrane show orders of magnitude higher density of defect states $N(E_F)$ and significantly smaller localization length *a* compared with those for NCO/STO and NCO/LAO. This result points to much higher disorder level in SAO buffered NCO films, which is preserved in NCO membranes.

5. Anomalous Hall Effect in $NiCo_2O_4/MgAl_2O_4$ Thin Film

Figure S9 shows the anomalous Hall effect (AHE) in a 30 nm NCO film on MAO. The anomalous Hall resistance exhibits robust switching hysteresis of clockwise direction at 260 K and 300 K, with coercive fields of about 500 Oe. The small coercive fields and square-shape hysteresis confirm that the NCO/MAO thin film exhibits strong perpendicular magnetic anisotropy even at room temperature.[7]

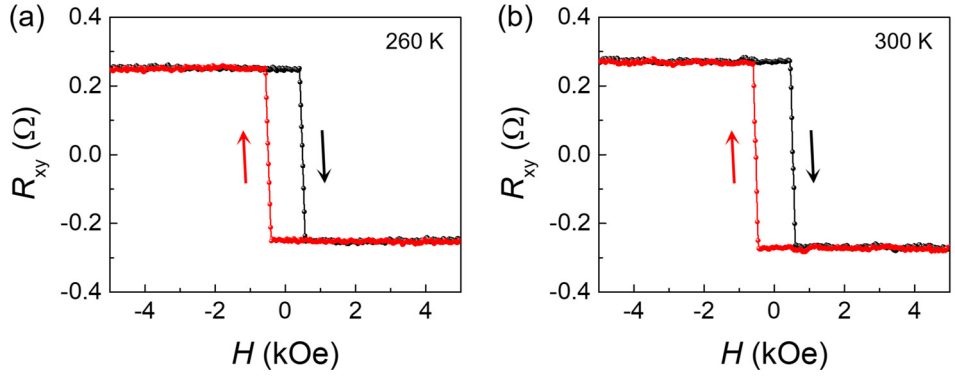

Figure S9. AHE of 30 nm NCO on MAO. (a-b) R_{xy} vs H at 260 K (a) and 300 K (b).

6. Magnetic Characterizations of $NiCo_2O_4$ Thin Films and Membranes

Figure S10 shows the magnetization switching hysteresis in out-of-plane magnetic field for NCO films on various substrates and $NiCo_2O_4$ membrane at 100 K, 260 K, and 300 K. The switching characteristic is consistent with the anomalous Hall effect (Figure 3 in the main text), showing perpendicular magnetic anisotropy for NCO on MAO and spin canting effect for NCO on perovskite substrates and NCO membranes.

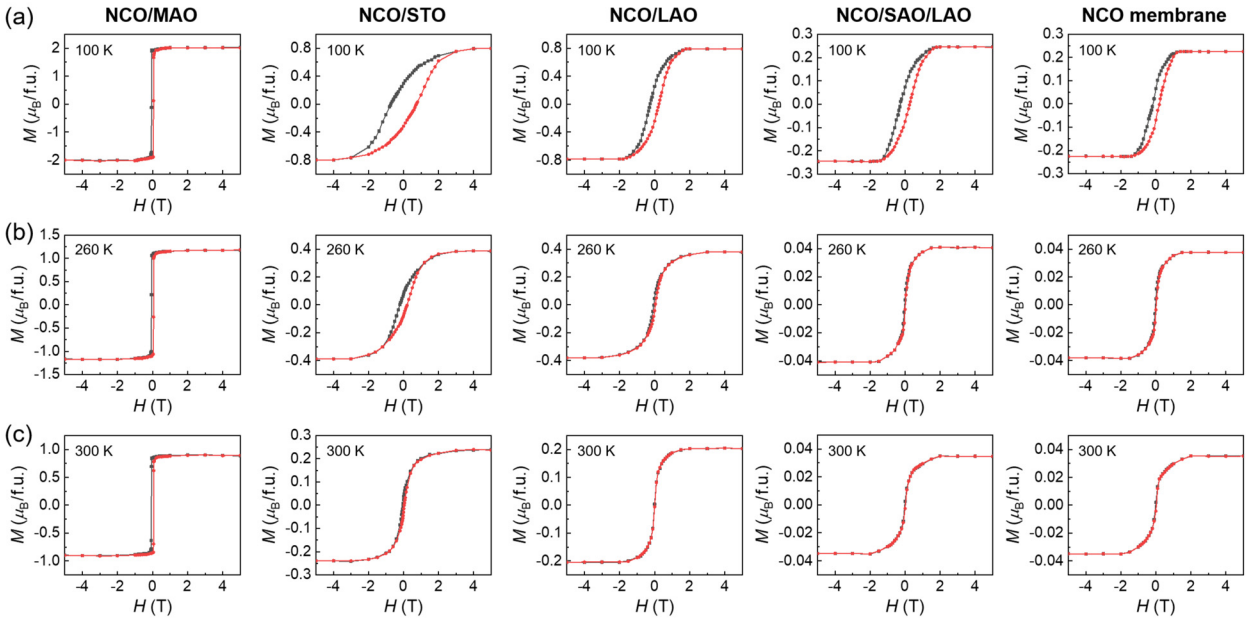

Figure S10. Magnetization hysteresis (M vs H) of NCO thin films and membrane at different temperatures. (a) 100 K. (b) 260 K. (c) 300 K.

7. Coherent Rotation Model for Two-Fold Sinusoidal AMR

In an isotropic non-crystalline magnetic conductor system, the electric field $\boldsymbol{E}$ is related to the current density $\boldsymbol{j}$ via the resistivity tensor:[8]

$$\begin{bmatrix} E_{x'} \\ E_{y'} \end{bmatrix} = \begin{bmatrix} \rho_{\parallel} & 0 \\ 0 & \rho_{\perp} \end{bmatrix} \begin{bmatrix} j_{x'} \\ j_{y'} \end{bmatrix},$$

where $\rho_{\parallel}$ and $\rho_{\perp}$ are the magnetoresistivity for current parallel with and perpendicular to the magnetic field, respectively. We assume that current makes an angle φ with respect to the in-plane magnetization, and the magnetization is aligned with the external applied magnetic field. When a rotation transformation is performed to the system:

$$R = \begin{bmatrix} \cos\varphi & -\sin\varphi \\ \sin\varphi & \cos\varphi \end{bmatrix},$$

we obtain:

$$R \begin{bmatrix} E_{x'} \\ E_{y'} \end{bmatrix} = R \begin{bmatrix} \rho_{\parallel} & 0 \\ 0 & \rho_{\perp} \end{bmatrix} R^{\dagger} R \begin{bmatrix} j_{x'} \\ j_{y'} \end{bmatrix}.$$

Let $\begin{bmatrix} E_x \\ E_y \end{bmatrix} = R \begin{bmatrix} E_{x'} \\ E_{y'} \end{bmatrix}$ and $\begin{bmatrix} j_x \\ j_y \end{bmatrix} = R \begin{bmatrix} j_{x'} \\ j_{y'} \end{bmatrix}$, we derive that:

$$\begin{bmatrix} E_x \\ E_y \end{bmatrix} = \begin{bmatrix} \frac{1}{2}(\rho_{\parallel}+\rho_{\perp}) + \frac{1}{2}(\rho_{\parallel}-\rho_{\perp})\cos 2\varphi & \frac{1}{2}(\rho_{\parallel}-\rho_{\perp})\sin 2\varphi \\ \frac{1}{2}(\rho_{\parallel}-\rho_{\perp})\sin 2\varphi & \frac{1}{2}(\rho_{\parallel}+\rho_{\perp}) + \frac{1}{2}(\rho_{\parallel}-\rho_{\perp})\cos 2\varphi \end{bmatrix} \begin{bmatrix} j_x \\ j_y \end{bmatrix}. \quad \text{(S3)}$$

From Equation S3, the angular dependences of the longitudinal magnetoresistance and transverse magnetoresistance, known as the anisotropic magnetoresistance (AMR) and planar Hall effect (PHE), respectively, are given by:

$$\rho_{\mathrm{AMR}}(\varphi) = \frac{1}{2}(\rho_{\parallel}+\rho_{\perp}) + \frac{1}{2}(\rho_{\parallel}-\rho_{\perp})\cos 2\varphi\,, \quad \text{(S4)}$$

$$\rho_{\mathrm{PHE}}(\varphi) = \frac{1}{2}(\rho_{\parallel}-\rho_{\perp})\sin 2\varphi\,. \quad \text{(S5)}$$

Equations S4 and S5 are also known as the Voigt-Thomson formula.[9] Generally, $\rho_{\parallel} \neq \rho_{\perp}$ in magnetic conductors. Within the coherent rotation model, where the magnetization follows the magnetic field direction, the AMR and PHE exhibit two-fold sinusoidal behaviors with a 45° phase shift with respect to each other.

8. In-plane AMR in $NiCo_2O_4$ Thin Films and Membranes

Figure S11 shows the angular dependence of in-plane AMR in 30 nm NCO on MAO. The AMR resistivity shows clear two-fold sinusoidal behaviors at the entire temperature (10-300 K) and magnetic field (0.25-3 T) ranges, consistent with the two-fold coherent rotation model.

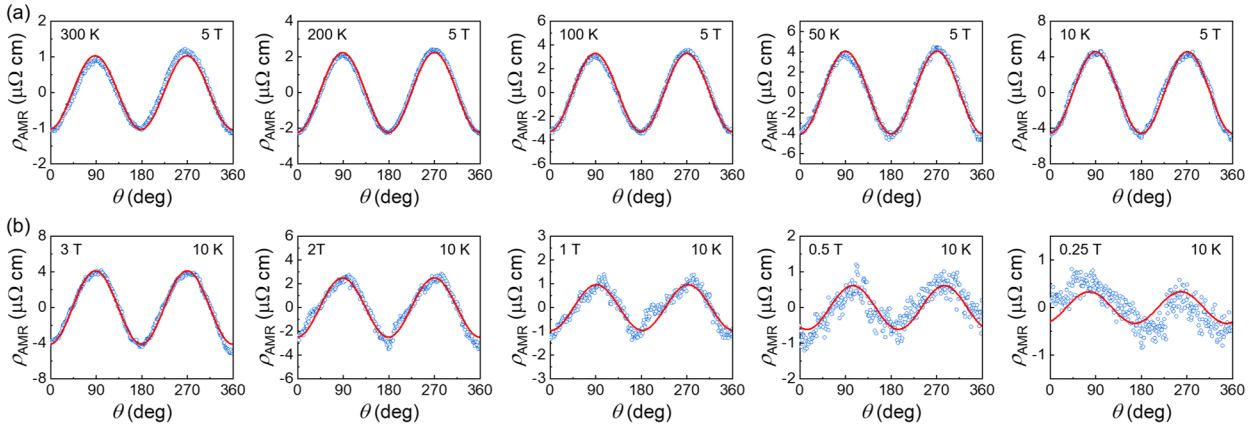

Figure S11. In-plane AMR for NCO/MAO. (a) ρ_{AMR} vs θ at 5 T and various temperatures, and (b) ρ_{AMR} vs θ at 10 K and various magnetic fields, with fits to the two-fold coherent rotation model (lines).

Figure S12 shows the angular dependence of in-plane AMR in 30 nm NCO films on STO, LAO, and SAO-buffered LAO and the NCO membrane at 5 T. For NCO/STO (Figure S12a), ρ_{AMR}

still shows a two-fold sinusoidal behavior at 300 K. When the temperature decreases, additional peaks emerge at $\theta = 0^{\circ}$ and $\theta = 180^{\circ}$, suggesting the appearance of a four-fold symmetric term. The amplitude of the four-fold term increases with decreasing temperature and becomes comparable with the two-fold component at 10 K. Similar temperature dependence of $\rho_{\mathrm{AMR}}(\theta)$ has been observed in NCO/LAO (Figure S12b).

For NCO/SAO/LAO (Figure S12c), ρ_{AMR} shows a one-fold symmetric behavior at 300 K, which can be attributed to the enhanced MR contribution as the temperature approaches the Curie temperature. As the temperature decreases to 200 K, $\rho_{\mathrm{AMR}}(\theta)$ recovers the two-fold sinusoidal behavior. The four-fold term appears below 150 K and increases with decreasing temperature. The NCO membrane shows almost identical AMR behavior as the NCO/SAO/LAO sample, suggesting the MCA and defect states are not altered after water etching of the SAO buffer layer.

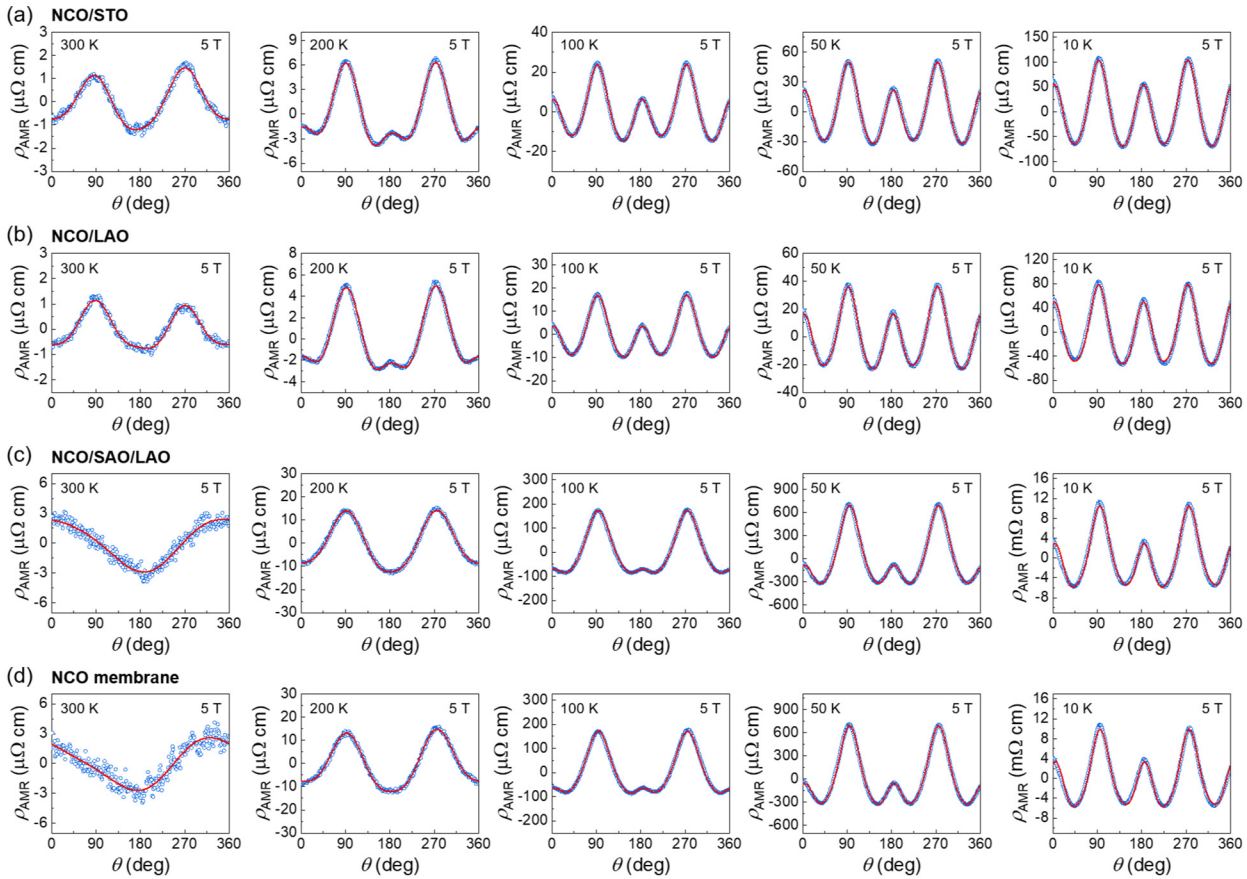

Figure S12. Angular-dependence of in-plane AMR $\rho_{\mathrm{AMR}}(\theta)$ at 5 T and various temperatures. (a) NCO/STO. (b) NCO/LAO. (c) NCO/SAO/LAO. (d) NCO membrane. The red lines are the fits. All data are taken on the forward θ-sweep.

Figure S13 shows the FFT spectra of $\rho_{\mathrm{AMR}}(\theta)$ in 30 nm NCO films on STO, LAO, and SAO-buffered LAO and the NCO membrane. The temperature dependences of the C_2 and C_4 components at 5 T (Figure S13a) are shown in Figure 6a-b in the main text. At 10 K, it is evident that besides the C_2 and C_4 terms, a one-fold $C_1(360°)$ term appears at low magnetic fields. Its amplitude increases with decreasing field and becomes dominant below 1 T (Figure S13b).

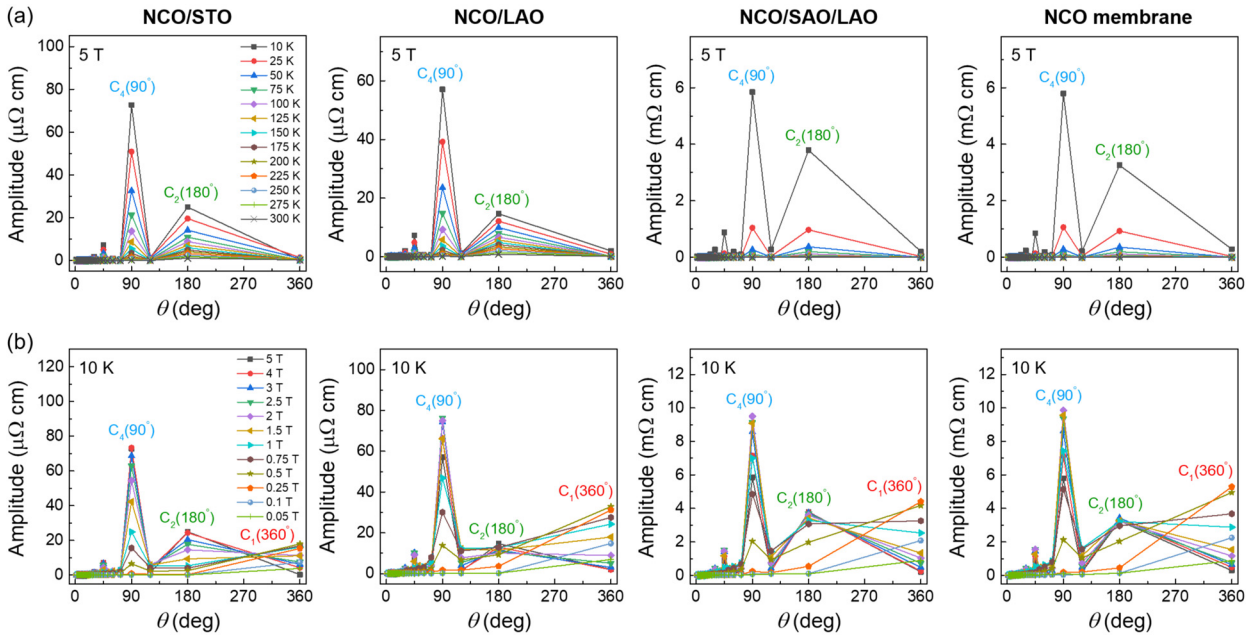

Figure S13. FFT spectrum of $\rho_{\mathrm{AMR}}(\theta)$ for NCO thin films and NCO membrane. (a) Amplitude vs θ at 5 T and different temperatures. (b) Amplitude vs θ at 10 K and different magnetic fields.

References

1. Zhen, C.; Zhang, X.; Wei, W.; Guo, W.; Pant, A.; Xu, X.; Shen, J.; Ma, L.; Hou, D., Nanostructural origin of semiconductivity and large magnetoresistance in epitaxial $NiCo_2O_4/Al_2O_3$ thin films. *Journal of Physics D: Applied Physics* **2018,** *51* (14), 145308.
2. Cabo, M.; Pellicer, E.; Rossinyol, E.; Castell, O.; Suriñach, S.; Baró, M. D., Mesoporous $NiCo_2O_4$ Spinel: Influence of Calcination Temperature over Phase Purity and Thermal Stability. *Crystal Growth & Design* **2009,** *9* (11), 4814-4821.
3. Xu, X.; Mellinger, C.; Cheng, Z. G.; Chen, X.; Hong, X., Epitaxial $NiCo_2O_4$ film as an emergent spintronic material: Magnetism and transport properties. *Journal of Applied Physics* **2022,** *132* (2), 020901.
4. Paul, D.; Mitra, S., Evaluation of Mott's parameters for hopping conduction in amorphous Ge, Si, and Se-Si. *Physical Review Letters* **1973,** *31* (16), 1000.
5. Jia, C.; Yang, F.; Zhao, L.; Cheng, G.; Yang, G., Temperature-dependent electrical transport properties of individual $NiCo_2O_4$ nanowire. *Nanoscale Research Letters* **2019,** *14* (1), 10.
6. Chen, X.; Wu, Q.; Zhang, L.; Hao, Y.; Han, M.-G.; Zhu, Y.; Hong, X., Anomalous Hall effect and perpendicular magnetic anisotropy in ultrathin ferrimagnetic $NiCo_2O_4$ films. *Applied Physics Letters* **2022,** *120* (24), 242401.
7. Chen, X.; Zhang, X.; Han, M. G.; Zhang, L.; Zhu, Y.; Xu, X.; Hong, X., Magnetotransport Anomaly in Room‐Temperature Ferrimagnetic $NiCo_2O_4$ Thin Films. *Advanced Materials* **2019,** *31* (4), 1805260.
8. Ritzinger, P.; Výborný, K., Anisotropic magnetoresistance: materials, models and applications. *Royal society open science* **2023,** *10* (10), 230564.
9. Jan, J.-P., Galvamomagnetic and thermomagnetic effects in metals; *Solid State Physics*; eds Frederick Seitz & David Tumbull; Academic Press: New York 1957; Vol. 5, pp 1-96.